Monitoring aerosols over Europe: an assessment of the potential benefit of assimilating the VIS04 measurements from the future MTG/FCI geostationary imager

Maxence Descheemaecker[1], Matthieu Plu[1], Virginie Marécal[1], Marine Claeyman[2], Francis Olivier[2], Youva Aoun[3], Philippe Blanc[3], Lucien Wald[3], Jonathan Guth[1], Bojan Sič[1], Jérôme Vidot[4], Andrea Piacentini[5], Béatrice Josse[1]

1CNRM, Université de Toulouse, Météo-France, CNRS, Toulouse, France
2Thales Alenia Space, Cannes la Bocca, 06156, France
3Mines ParisTech, PSL Research University, O.I.E.- Center for Observation, Impacts, Energy, Sophia Antipolis, 06904, France
4Centre de Météorologie Spatiale, Météo-France, 22300, Lannion, France
5CERFACS – CNRS, UMR5318, 31057, Toulouse, France

Correspondence to: Maxence Descheemaecker (maxence.descheemaecker@meteo.fr)

Abstract. The study assesses the possible benefit of assimilating Aerosol Optical Depth (AOD) from the future spaceborne sensor FCI (Flexible Combined Imager) for air quality monitoring in Europe. An Observing System Simulation Experiment (OSSE) was designed and applied over a 4-month period that includes a severe pollution episode. The study focuses on the FCI channel centred at 444 nm, which is the shortest wavelength of FCI. A Nature Run (NR) and four different Control Runs of the MOCAGE chemistry-transport model were designed and evaluated to guarantee the robustness of the OSSE results. The AOD synthetic observations from the NR were disturbed by errors that are typical of the FCI. The variance of the FCI AOD at 444 nm was deduced from a global sensitivity analysis that took into account the aerosol type, surface reflectance and different atmospheric optical properties. The experiments show a general benefit on all statistical indicators of the assimilation of the FCI AOD at 444 nm for aerosol concentrations at surface over Europe, and also a positive impact during the severe pollution event. The simulations with data assimilation reproduced spatial and temporal patterns of PM_{10} concentrations at surface better than without assimilation all along the simulations and especially during the pollution event. The advantage of assimilating AOD from a geostationary platform over a Low Earth Orbit satellite has also been quantified. This work demonstrates the capability of data from the future FCI sensor to bring an added value to the MOCAGE aerosol simulations, and in general, to other chemistry transport models.

1 Introduction

Aerosols are liquid and solid compounds suspended in the atmosphere, whose sizes range from a few nanometers to several tens of micrometers, and whose lifetime in the troposphere varies from a few hours to a few weeks (Seinfeld and Pandis, 1998). Stable sulfate aerosols at high altitude can last for years (Chazette et al., 1995). The sources of aerosols may be natural (dusts, sea salt, ashes from volcanic eruptions, for instance) or anthropogenic (from road traffic, residential heating, industries, for instance), and they can be transported up to thousands of kilometers. Aerosols are known to have significant impacts on climate (IPCC, 2007) and on air quality and further on human health as WHO (2014) estimated over 3 million deaths in 2012 to be due to aerosols.

Aerosols absorb and diffuse solar radiation, which leads to local heating of the aerosol layer and cooling of the climate system through the backscatter of solar radiation to space for most of the aerosols, except for black carbon (Stocker et al., 2013). The absorption of solar radiation modifies the vertical temperature profile, affecting the stability of the atmosphere and cloud formation (Seinfeld and Pandis, 1998). Aerosols, as condensation nuclei, play a significant role in the formation and life cycle of clouds (Seinfeld and Pandis, 1998). Deposition of aerosols on Earth's surface may also affect surface properties and albedo. All these effects show that aerosols play a key role on the energy budget of the climate system.

Aerosols, also called particulate matter in the context of air quality, are responsible for serious health problems all over the world, as they are known to favor respiratory and cardiovascular diseases as well as cancers (Brook et al., 2004). The World Health Organization (WHO) has set regulatory limits for aerosol concentrations, respectively 20 μg.m^{-3} and 10 μg.m^{-3} annual mean for PM$_{10}$ and PM$_{2.5}$ (particulate matter with a diameter less than 10 and 2.5 μm, respectively) concentrations. The European Union regulation introduces also PM$_{10}$ daily mean limits of 50 μg.m^{-3}. The presence of a dense layer of aerosols can also affect air traffic by the reduction of visibility (Bäumer et al., 2008) and by risks of disruptions of engines of air planes (Guffanti et al., 2010). Therefore, it is essential to accurately determine the evolution of the concentration and size of the different types of aerosols in space and time, in order to assess their effect on climate and on air quality and to mitigate their impacts. A pertinent approach to achieve a continuous and accurate monitoring of aerosols is to combine measurements and models, a good example being the Copernicus Atmosphere Monitoring Service (CAMS) (http://www.atmosphere.copernicus.eu/; Peuch and Engelen, 2012; Eskes et al., 2015; Marécal et al, 2015).

Ground-based stations, which measure aerosol and gas concentrations in-situ, have been used for several decades to monitor air quality, such as the stations in the Air Quality e-Reporting program (AQeR, https://www.eea.europa.eu/data-and-maps/data/aqereporting-2) from the European Environment Agency (EEA). Other observations can also be used to measure aerosols. The AERONET (AErosol RObotic NETwork) program (https://aeronet.gsfc.nasa.gov/) performs the retrieval of the Aerosol Optical Depth (AOD) at several ground stations (Holben et al., 1998). Similarly, AOD observations can be retrieved from images taken in different channels by imagers aboard Low Earth Orbit (LEO) or GEOstationary (GEO) satellites. Generally, AOD from satellite provides a better spatial coverage than ground-based stations at the expense of additional sources of uncertainty, such as the surface reflectance. An example of AOD product from LEO satellites is the Daily Level 2

AOD, from the Moderate Resolution Imaging Spectroradiometer (MODIS) (Levy et al., 2013) sensor on board Terra and Aqua (MOD 04 & MYD 04 products). This AOD product is provided at a 10 km resolution every 5 min, down to 1 km. Sensors on geostationary orbit satellites can continuously scan one third of Earth's surface much more frequently than low Earth orbit satellites. The SEVIRI (Spinning Enhanced Visible and Infra-Red Imager) sensor, aboard MSG (Meteosat

5 Second Generation), is an example of a GEO sensor providing information on aerosols. Different AOD are retrieved over lands from SEVIRI data in the VIS0.6 and VIS0.8 channels, respectively centered at 0.635 µm (0.56 µm – 0.71 µm) and 0.81 µm (0.74 µm – 0.88µm). AOD products are retrieved following different methods. Carrer et al. (2010) presented a method to estimate a daily quality-controlled AOD based on a directional and temporal analysis of SEVIRI observations of channel VIS0.6. Another method consists in matching simulated Top Of the Atmosphere (TOA) reflectances (from a set of 5

10 models) with TOA SEVIRI reflectances (Bernard et al., 2011) to obtain an AOD for VIS0.6. Another method (Mei et al., 2012) estimates the AOD and the aerosol type by analysing the reflectances at 0.6 and 0.8 µm in three orderly scan times. These methods derive AOD for specific channels, from the combined analysis of several channels and very often using several images if not all of a day to have information.

Numerical models, even if they are subject to errors, are necessary to describe the variability of the aerosol types and of their

15 concentrations with space and time, as a complement to observations. Aerosol forecasts on regional and global scales are made by three-dimensional models, such as the chemistry-transport model (CTM) MOCAGE (Sič et al., 2015; Guth et al., 2016). MOCAGE is currently used daily to provide air quality forecasts to the French platform Prev'Air (Rouil et al., 2009) and also to the European CAMS ensemble (Marécal et al., 2015). Data assimilation of AOD can be used in order to improve the representation of aerosols within the model simulations (Benedetti et al, 2009, Sič et al, 2016). Studies on geostationary

20 sensors have also proved a positive effect of the assimilation of AOD, see e.g. Yumimoto, et al. (2016), who assessed this positive effect using the AOD at 550 nm from AHI (Advanced Himawari Imager) sensor aboard Himawari-8.

The future geostationary Flexible Combined Imager (FCI, URD Eumetsat, 2010), that will be aboard the Meteosat Third Generation satellite (MTG), will perform a full disk in 10 min, and in 2.5 min for the European Regional-Rapid-Scan which covers one-quarter of the full disk, with a spatial resolution of 1 km at nadir and around 2 km in Europe. Like AHI, FCI is

25 designed to have multiple wavelengths and the assimilation of its data into models should be beneficial to aerosol monitoring. The aim of the paper is to assess the possible benefit of assimilating measurements from the future MTG/FCI sensor for monitoring aerosols on regional scale over Europe. Since MOCAGE cannot assimilate, AOD at multiple wavelengths simultaneously (Sič et al, 2016), the study focusses on the assimilation of AOD from a single channel. Among the 16 channels of FCI, the VIS04 band (centered at 444 nm) has been chosen because it covers the shortest wavelengths,

30 which is expected to be the most relevant to detect small particles (Petty, 2006). Besides, VIS04 is a new channel compared to MSG/SEVIRI, which shortest band is around 650nm (Carrer et al, 2010), and so assessing the benefit of VIS04 over Europe is original.

As FCI is not yet operational, an OSSE (Observing System Simulation Experiments) approach (Timmermans et al., 2015) is used in this study. In an OSSE, synthetic observations are created from a numerical simulation that is as close as possible to

the real atmosphere (the Nature Run), and then are assimilated in a different model configuration. The differences between model outputs with and without assimilation provide an assessment of the added value of the assimilated data. OSSE have been widely developed and used for assessing and designing future sensors for air quality monitoring: for carbon monoxide (Edwards et al, 2009) and ozone (Claeyman et al, 2011; Zoogman et al, 2014) from LEO or GEO satellites (Lahoz et al,

5 2012), and for aerosol analysis from GEO satellites over Europe (Timmermans et al, 2009a, 2009b). Some of these studies have successfully assessed the potential benefit of future satellites and they have helped to design the instruments (Claeyman et al, 2011), however cautions and limitations on the OSSE for air quality have been addressed (Timmermans et al, 2009a, 2009b, 2015), such as the "identical twin problem" and the control of the boundary conditions of the model, and the accuracy and the representativeness of the synthetic observations.

10 By designing an OSSE that takes into account these precautions, the present study proposes a quantitative assessment of the potential benefit of assimilating AOD at 444 nm from FCI for aerosol monitoring in Europe. The OSSE and its experimental setup are described in Sect. 2. Then, the case study and an evaluation of the ability of the reference simulation to represent a true state of the atmosphere are presented. The calculation of synthetic observations is explained in Sect. 3. An evaluation of the control simulations is made in Sect. 4. In Sect. 5, the results of the assimilation of FCI synthetic observations are

15 presented and discussed. Finally, Sect. 6 concludes this study.

2 Methodology

2.1 Experimental setup

Figure 1 shows the general principle of the OSSE (Timmermans et al, 2015). A reference simulation, called "Nature Run" (NR) is assumed to represent the "true" state of the atmosphere. AOD synthetic observations are generated by combining

20 AOD retrieved from the NR and the error characteristics of FCI. These error characteristics are described in Sect. 3. The second kind of simulations in the OSSE is the "Control Run" (CR) simulation. The differences between NR's output and CR's output should represent the errors of current models without use of observations. Finally, the assimilation run (AR) is done by assimilation in the CR of the synthetic observations. To assess the added value of the instrument, a comparison is made between the output of the AR and the NR and between the CR and the NR. If the AR is closer to the NR than the CR,

25 it means that the observations provide useful information to the assimilation system. The differences between AR and CR quantify the added value of the instrument.

The NR should be as close as possible to the actual atmosphere because it serves as the reference to produce the synthetic observations. The temporal and spatial variations of the NR should approximate those of actual observations. An evaluation of the NR, presented in Sect. 2.2, includes a comparison of the model with aerosol concentrations and AOD data from

30 ground-based stations.

In addition, the differences between the NR and the CR must be significant and approximate those between the CR and the actual observations. Ideally, the NR and CR should be run with different models, as the use of the same model could lead to

4

over-optimistic results (Masutani et al., 2010); this issue is called the "identical twin" problem. It is strongly recommended to evaluate the spatio-temporal variability of the NR and its differences with the CR to avoid this "identical twin" problem (Timmermans et al., 2015). As MOCAGE is used for both NR and CR in the present study, a method similar to that used in Claeyman et al. (2011) is proposed. Instead of one CR, various CR simulations (Fig. 1) are performed in different
5   configurations, and they are assessed independently and compared to the NR to ensure the robustness of the OSSE results. An evaluation of those differences is presented in Sect. 4.

2.2 MOCAGE

The CTM model used in this study is MOCAGE (Modèle de Chimie Atmosphérique à Grande Echelle, Guth et al, 2016), that has been developed for operational and research purposes. MOCAGE is a three-dimensional model that covers the
10 global scale, down to regional scale using two-way nested grids. MOCAGE vertical resolution is not uniform: the model has 47 vertical sigma-hybrid altitude-pressure levels from the surface up to 5 hPa. Levels are denser near the surface, with a resolution of about 40 m in the lower troposphere and 800 m in the lower stratosphere.

MOCAGE simulates gases (Josse et al., 2004; Dufour et al., 2004), primary aerosols (Martet et al., 2009; Sič et al., 2015) and secondary inorganic aerosols (Guth et al, 2016). Aerosols species in the model are primary species: desert dust, sea salt,
15 black carbon and organic carbon, and secondary inorganic species: sulfate, nitrate and ammonium, formed from gaseous precursors in the model. For each type of aerosols (primary and secondary), the same 6 bin sizes are used between 2 nm and 50 µm: 2 nm -10 nm - 100 nm - 1 µm - 2.5 µm - 10 µm - 50 µm. All emitted species are injected every 15 mins in the five lower levels (up to 0.5 km), following an hyperbolic decay with altitude: the fraction of pollutants emitted in the lowest level is 52 %, and then respectively 26 %, 13 %, 6 % and 3 % in the four levels above. Such a vertical repartition ensures
20 continuous concentration fields in the first levels, which guarantee a proper behavior of the of the semi-Lagrangian advection scheme. Carbonaceous particles are emitted using emission inventories. Sea salt emissions are simulated using a semi-empirical source function (Gong, 2003; Jaeglé et al., 2011) with the wind speed and the water temperature as input. Desert dust are emitted, using wind speed, soil moisture and surface characteristics based on Marticorena and Bergametti (1995) which give the total emission mass, that is then distributed in each bin according to Alfaro et al. (1998). Secondary inorganic
25 aerosols are included in MOCAGE using the module ISORROPIA II (Fountoukis and Nenes, 2007), which solves the thermodynamic equilibrium between gaseous, liquid and solid compounds. Chemical species are transformed by the RACMOBUS scheme, which is a combination of the RACM scheme (Regional Atmospheric Chemistry Mechanism; Stockwell et al., 1997) and the REPROBUS scheme (Reactive Processes Ruling the Ozone Budget in the Stratosphere; Lefèvre et al., 1994). Dry and wet depositions of gaseous and particulate compounds are parameterized as in Guth et al.
30 (2016).

MOCAGE uses meteorological forecasts (wind, pressure, temperature, specific humidity, precipitation) as input, such as Météo-France operational meteorological forecast from ARPEGE (Action de Recherche Petite Echelle Grande Echelle), or ECMWF (European Centre for Medium-Range Weather Forecasts) meteorological forecast from IFS (Integrated Forecast

System). A semi-lagrangian advection scheme (Williamson and Rasch, 1989), a parameterization for convection (Bechtold et al., 2001) and a diffusion scheme (Louis, 1979) are used to transport gaseous and particulate species.

2.3 Assimilation system PALM

The assimilation system of MOCAGE (Massart et al., 2009), is based on the 3-Dimensional First Guess at Appropriate Time
5 (3D-FGAT) algorithm. This method consists of minimizing the cost function J:

$$J(\delta x) = J_b(\delta x) + J_o(\delta x) = \frac{1}{2}(\delta x)^T \boldsymbol{B^{-1}} \delta x + \frac{1}{2}\sum_{i=0}^{N}(d_i - \boldsymbol{H_i}\delta x)^T \boldsymbol{R_i^{-1}}(d_i - \boldsymbol{H_i}\delta x), \tag{1}$$

where J_b and J_o are respectively the part of the cost function related to the model background and to the observations; $\delta x = x - x^b$ is the difference between the model background x^b and the state of the system x; $d_i = y_i - H_i x^b(t_i)$ is the difference between the observation y_i and the background x^b in the observations space at time t_i; H_i is the observation operator; $\mathbf{H}$ its
10 linearized version; $\mathbf{B}$ is the background covariance matrix; and $\mathbf{R_i}$ is the observation covariance matrix at time t_i.

The general principal for the assimilation of AOD (Benedetti et al, 2009) is the same as in Sič et al. (2016). The control variable x used in the minimization is the 3D total aerosol concentration. After minimization of the cost function, an analysis increment δx^a, is obtained, which is a 3D-total aerosol concentration. This increment δx^a is then converted into all MOCAGE aerosol bins according to their local fractions of the total aerosol mass in the model background. The result is added to the
15 background aerosol field at the beginning of the cycle. Then the model is run over the 1-hour cycle length to obtain the analysis. The state at the end of this cycle is used as a departure point for the background model run of the next cycle.

The observation operator $\mathbf{H}$ for AOD uses as input the concentrations of all bins (6) of the seven types of aerosols and the associated optical properties. For this computation also, the control variable x is converted into all MOCAGE aerosol bins according to their local fractions of the total aerosol mass in the model background. The AOD is computed for each model
20 layer to obtain, by summing, the AOD of the total column. The optical properties of the different aerosol types are issued from a look-up table, that is computed from the Mie code scheme of Wiscombe (1980, 1979, revised 1996) for spherical and homogeneous particles. The refractive indices come from Kirchstetter et al. (2004) for organic carbon and from the Global Aerosol Data Set (GADS, Köpke et al., 1997) for other aerosol species. The hygroscopicity of sea salts and secondary inorganic aerosols are taken into account based on Gerber (1985).

25 While the observation operator is designed to assimilate AOD of any wavelength from the UV to the IR, the assimilation system MOCAGE-PALM cannot assimilate data of several wavelengths simultaneously (Sič et al, 2016). This limitation is due to the choice of the control vector, which is the 3D total aerosol concentration: assimilating different wavelengths simultaneously would require to rethink and to extend the control vector, for instance splitting it by aerosol size bins or types. This explains why the study focuses on the assimilation of AOD of a single wavelength.

6

2.4 Case study

The period extends from the 1st of January to the 30th of April 2014, and includes several days of PM pollution over Europe. From the 7th to 15th of March, a secondary particles episode (EEA report 2014) occurs, while from 29th March to 5th April a dust plume originating from the Sahara Desert propagates Northwards to Europe (Vieno et al., 2016).

5 The MOCAGE simulation covers the whole period from January to April 2014, on a global domain at 2° resolution and a nested regional domain, that covers Europe, from 28 °N to 72 °N and from 26 °W to 46 °E, at 0.2 ° resolution (see Fig. 2). A 4-month spin-up is made before the simulation. The NR is forced by ARPEGE meteorological analysis. Emissions of chemical species in the global domain come from MACCity (van der Werf et al., 2006; Lamarque et al., 2010; Granier et al., 2011) for anthropogenic gas species and biogenic species are from GEIA for the global and regional domain. ACCMIP
10 project emissions are used for anthropogenic organic and black carbon emissions at the global scale. The TNO-MACC-III inventory for year 2011 provides anthropogenic emissions in the regional domain. TNO-MACC-III emissions are the latest update of the TNO-MACC inventory based on the methodology developed in the MACC-II project described in Kuenen et al. (2014). These anthropogenic emissions are completed, on our regional domain, at the boundary of the MACC-III inventory domain by emissions from MACCity. Daily biomass burning sources of organic and black carbon and gases from
15 the Global Fire Assimilation System (GFAS) (Kaiser et al., 2012) are injected in the model. The NR includes secondary organic aerosols (SOA) in order to enhance its realism and to well fit the observations made at ground-based stations over Europe. Standard ratios from observations (Castro et al., 1999) are used to simulate the portion of secondary carbon species, 40 % in winter, from the primary carbon species in the emission input.

The NR is compared to real observations from AERONET AOD observations and AQeR surface concentrations, using
20 common statistical indicators: mean bias (B), modified normalized mean bias (MNMB), root mean square error (RMSE), fractional gross error (FGE), Pearson correlation coefficient (R_p) and Spearman correlation coefficient (R_s). While the Pearson correlation measures the linear relation between the two datasets, the Spearman correlation is a mean to assess their monotonic relationship.

The AQeR stations are mainly located over Western Europe (Fig. 2). After selection of the surface stations that are
25 representative of background air pollution (following Joly and Peuch, 2012), 597 and 535 stations are respectively used for the PM$_{10}$, PM$_{2.5}$ comparison. Figure 2 represents the mean surface concentration of the NR and selected AQeR measurements over the domain, from January to April 2014. The left panel shows the PM$_{10}$ concentrations of the NR in the background and the AQeR concentrations as circle, while the right panel shows the PM$_{2.5}$ concentrations. The concentration of the NR PM$_{10}$ and PM$_{2.5}$ are generally underestimated compared to observations. Nevertheless, on both figures, the spatial
30 variability and particularly the location of maxima are reasonably well represented. Over the European continent, the NR and AQeR data show clear maxima in the center of Europe for both PM$_{10}$ and PM$_{2.5}$ concentrations, even if the NR underestimates these maxima.

Table 1 shows the statistical indicators of this comparison for hourly surface concentrations in PM_{10} and $PM_{2.5}$. A negative mean bias is observed, around -6.23 µg.m^{-3} (~ -35.1 %) for PM_{10} and -3.20 µg.m^{-3} (~ -24.7 %) for $PM_{2.5}$. The RMSE is equal to 16.2 µg.m^{-3} for PM_{10} and 11.9 µg.m^{-3} for $PM_{2.5}$ while the FGE equals to 0.56 and 0.543. The factor of two is equal to 64.7 % and 67.5 % for PM_{10} and $PM_{2.5}$. Pearson and Spearman correlations are respectively 0.452 and 0.535 for PM_{10} and $PM_{2.5}$ and 0.537 and 0.602 for PM_{10} and $PM_{2.5}$. The NR underestimation is greater for PM_{10} than for $PM_{2.5}$ in relative differences. This suggests a lack of aerosol concentrations in the $PM_{10-2.5}$ (concentration of aerosols between 2.5 µm and 10 µm). Not taking into account wind-blown crustal aerosols may cause a potential underestimation of PM in models (Im et al., 2015). Taking them into account needs a detailed ground type inventory to compute those emissions unavailable in MOCAGE. For $PM_{2.5}$, the underestimation of aerosol concentrations can be due to a lack of carbonaceous species (Prank et al., 2016). Other possible reasons for PM negative bias at surface are the underestimation of emissions in cold winter period and the uncertainty in the modelling of stable winter conditions with shallow surface layers.

A time-series graph of the median NR surface concentrations and the median surface concentrations of the AQeR stations are presented in Fig. 3. Compared to ground-based AQeR data (in black), the NR (in purple) generally underestimates the PM_{10} and the $PM_{2.5}$ concentrations, especially during the 7th-15th March pollution episode. However, the variations and maxima of the NR concentrations of PM are generally well represented. Furthermore, around 65 % of model concentrations are relatively close to observations as shown by the factor of 2 in Table 1. The variability of NR concentrations is thus consistent with AQeR station concentrations.

Table 2 gives an evaluation of the NR against the daily mean of the AOD at 500 nm obtained from 84 AERONET stations in the regional domain from January to April 2014. The statistical indicators show good consistency between the NR and AERONET observations. However, like the results showed at global scale (Sič et al, 2015), MOCAGE tends to overestimate AOD: although small, the AOD bias is positive. While PM concentrations at surface are underestimated in the NR, different reasons may explain an overestimation of AOD. The vertical distribution of aerosol concentrations in the model is largely controlled by vertical transport, removal processes and by the prior assumptions done on the aerosol emission profiles. However, these processes may have large variability and they are prone to large uncertainties (Sič et al, 2015). Another possible explanation is the uncertainty of the size distribution of aerosols that can affect significantly the optical properties. More generally, the assumptions that underly the computation of optical properties are largely uncertain and they can affect the computation of AOD by a factor of 50% (Curci et al, 2015): the mixing state assumption, the uncertainty on refractive indices and on hygrocopicity growth. These uncertainties on aerosol vertical profiles, size distribution, and optical properties may explain the decorrelation between AOD and PM concentrations at surface, and so why the MOCAGE NR has a positive bias in AOD while underestimating PM at surface. However, both the PM and AOD correlation errors of the NR remain in a realistic range.

As a result, the NR simulation exhibits surface concentrations and AOD in the same range compared to those from ground-based stations and shows similar spatial and temporal variations, which makes the NR acceptable for the OSSE.

3 Generation of synthetic AOD observations

The study focuses on the added value of assimilating AOD at the central wavelength (444 nm) of the FCI/VIS04 spectral band. Since the assimilation of AOD from several wavelengths simultaneously is not possible (Sect. 2.3), the choice of the single channel VIS04 is mainly driven by the fact that it is the shortest wavelengths of FCI, that is a priori the most favorable to the detection of fine particles.

Thus, synthetic AOD observations at 444nm are created over the MOCAGE simulated regional domain, from the NR simulation 3D fields: all aerosol concentrations per type and per size bins, and meteorological variables. At every gridpoint of the NR regional domain where the solar zenithal angle is below 80° (daytime) and where clouds are absent, an AOD value at 444 nm is computed using the MOCAGE observation operator described above (Sect. 2.3). In order to take into account the error characteristics of the FCI VIS04 AOD, a random noise is then added to this NR AOD value.

To estimate the variance of this random noise, the general principle is to assess and quantify the respective sensitivity of the FCI VIS04 top-of-the-atmosphere reflectance to AOD and to the other variables. For doing this, the FCI simulator developed by Aoun et al (2016), based on the Radiative Transfer Model (RTM) libRadtran (Mayer and Killings, 2005), has been used. This simulator computes the reflectance in the different spectral bands of FCI, as a function of different input atmospheric parameters (AOD τ, total column water vapor, ozone content), ground albedo ρ_g and solar zenithal angle θ_S, for different OPAC (Optical Properties of Aerosols and Clouds, Hess et al., 1998) aerosol types: dust, maritime clean, maritime polluted, continental clean, continental average, continental polluted, and urban.. The FCI simulator takes into account the spectral response sensitivity and the measurement noise representative of the FCI VIS04 spectral band (415-475 nm).

By applying a Global Sensitivity Analysis to this FCI simulator ran on a large dataset (see the Appendix for the details of the method), a look-up table of the RMSE of AOD is derived. It depends on the OPAC type, on the relative error of surface albedo, on the solar zenithal angle and of the ground albedo value. The classification of each MOCAGE profile into the OPAC types relies on three parameters (Tab. 3): the surface concentration, the main surface species and the proportion in relation to the total aerosols concentrations. A species is described as a main species if its concentrations, [species], is above each other concentrations, for example DD is a main species if [DD]>[SS] & [DD]>[IWS]. An example of NR profiles (7th March 2014 at 12 UTC) decomposed in OPAC type is presented in Fig. 4. A small part of the profiles are dismissed where MOCAGE profiles do not match one of the OPAC types, such as profiles over ocean where *IWS* (Insoluble, Water Soluble and Soot; Tab. 3) is greater than DD (Desert Dust) and SS (Sea Salt). A larger part of profiles are dismissed because of night-time profiles and cloudy conditions. Figure 5 represents the average number of NR AOD that are retained per day for assimilation. After these filters apply, between 10 % and 20 % of profiles are kept every hour. The density of these profiles is higher in the south of the domain, which is directly correlated to the quantity of direct sunlight available. Over the continent, between 1 and 4 profiles can be assimilated per day at each grid-box location.

9

On every NR profiles that is kept, an AOD error is introduced, by addition of random value from an unbiased Gaussian with a standard deviation derived from the AOD RMSE look-up table, calculated as explained above. The surface albedo fields are taken from MODIS using the Radiative Transfer Model RTTOV (Vidot et al., 2014). A relative error of 10% is assumed for ground albedo, which corresponds to a realistic value (Vidot et al, 2014). An example of the synthetic observations is presented in Fig. 6. It represents the NR AOD, the synthetic observations and the noise applied to NR AOD for the 7th March 2014 at 12 UTC.

4 Controls runs (CRs) and their comparison to NR

Sect. 2 showed an evaluation of the NR compared to real observations. Another requirement of the OSSE is the evaluation of differences between the NR and the CR. Various CR simulations have been performed to evaluate the behaviour of the OSSE on different CR configurations and prove its robustness. The NR and CRs use different setups of MOCAGE. The CRs use IFS meteorological forcings, while the NR uses ARPEGE meteorological forcings. The use of different meteorological inputs is expected to yield differences in the transport of pollutant species, and changes in dynamic emissions of sea salt and desert dust. To introduce more differences between the CRs and NR, changes in the emissions are also introduced.

Table 4 indicates the changes made on the different model parameters to create 4 distinct CR simulations. The first control run, CR1, uses the same inputs as the NR except for the meteorological forcings. Other control runs (CR2, CR3, CR4) do not have the SOA formation process of the NR (Sect. 2) and CR1 simulations. Finally, CR3 and CR4 change from other simulations by different vertical repartitions of emissions in the five lowest levels. In CR3, the pollutants are emitted with a slower decay with height than the NR (with repartition from 30 % at surface and respectively 24 %; 19 %; 15 %; 12 % for the four levels above), and in the CR4 emissions are only injected in the lowest level. These changes aim to generate simulations that are more significantly different from the NR than the first two control runs.

The four CRs are compared to the NR for PM_{10} and $PM_{2.5}$ surface concentration considering virtual observations located at the same locations as the AQeR stations. A time-series of daily means of surface concentrations at simulated stations is presented in Fig. 7, for NR and CRs simulations from the 1st January to the 30th April 2014. The PM_{10} concentrations of the NR (in purple) are mostly greater than the PM_{10} concentrations in the CRs. During the period of late March and early April (around the 90th day of simulation) the NR concentrations of PM_{10} are close to those of the CR2, CR3 and CR4, and less than those of the CR1 by about few μgm^{-3}. In terms of $PM_{2.5}$, the CRs concentrations are also underestimating the NR concentration. As for PM_{10}, around the 90th day of simulation, the concentrations of CR1 are above the concentrations of the NR.

These tendencies can also be observed in Fig. 8, which represents a scatter plot of CRs concentrations as a function of NR concentrations for the daily means of surface concentration in PM_{10} and $PM_{2.5}$ at the virtual stations. The CR1 concentrations are fairly close to those of the NR concentrations with a coefficient of regression about 0.801 and 0.835 for PM_{10} and $PM_{2.5}$. Other CRs underestimate the NR concentrations. This tendency is stronger for PM_{10} than for $PM_{2.5}$. The regression

coefficient of the CR2, CR3, CR4 are respectively 0.596, 0.583 and 0.607 for PM_{10} and 0.570, 0.505 0.647 for $PM_{2.5}$. For both PM_{10} and $PM_{2.5}$ concentrations, the underestimation is more important for high values of the NR concentrations than for low values.

The statistical indicators in Tab. 5 and 6 are consistent with Fig. 7 and 8. The CR1 is close to the NR with a bias of -1.3
5 (-8.2 %) $\mu g.m^{-3}$ for PM_{10} and -0.8 (-6.2 %) $\mu g.m^{-3}$ for $PM_{2.5}$. CR4 bias is around -2.9 (-20.5 %) $\mu g.m^{-3}$ for PM_{10} and -1.8 (-15.1 %) $\mu g.m^{-3}$ for $PM_{2.5}$. The two other CRs highly underestimate PM_{10} and $PM_{2.5}$ concentrations with a bias of -4.5 $\mu g.m^{-3}$ (-35.2 %) and -3.9 $\mu g.m^{-3}$ (-37.4 %) respectively for CR2 and -4.8 $\mu g.m^{-3}$ (-38.1 %) and -4.4 $\mu g.m^{-3}$ (-42.6 %) for the CR3. These biases are in agreement with the literature. Prank et al. (2016) measure a bias around -5.8 for PM_{10} and -4.4 $\mu g.m^{-3}$ for $PM_{2.5}$ for the median of four CTMs against ground-based stations in winter. In Marécal et al. (2015), statistical indicators for
10 an ensemble of seven models are presented for winter. A bias between -3 and -7 $\mu g.m^{-3}$ is observed for the median ensemble. The PM concentrations of our CRs compared to the NR are characteristic of models compared to observations.

Prank et al. (2016) also show other indicators for the median of models, such as the temporal correlation and the factor of 2. Their correlations are around 0.7 for $PM_{2.5}$ and 0.6 for PM_{10} and are close to those for our CRs simulations that vary from 0.644 to 0.732 for $PM_{2.5}$ and from 0.572 to 0.671 for PM_{10}. Their factor of 2 equals 65 % for PM_{10} and 67 % for $PM_{2.5}$. The
15 factor of 2 of the CRs ranges between 70 % and 90 % for both PM_{10} and $PM_{2.5}$ concentrations. The RMSE of CRs simulations ranges from 8 $\mu g.m^{-3}$ to 10 $\mu g.m^{-3}$ for PM_{10} concentrations, which is slightly under the RMSE of the ensemble from the study of Marécal et al. (2015) which ranges between 10 and 15 $\mu g.m^{-3}$. The FGE of the study of Marécal et al. is equal to 0.55, while the FGE of CRs varies from 0.33 to 0.51. Our CRs simulations slightly underestimate the model relative error. Thus, compared to literature, the CRs (especially the CR3) are different enough from the NR to be representative of
20 state-of-the-art simulations.,

Between the CRs and the NR there are important spatial differences in surface concentrations of PM, as demonstrated in Fig. 9, which shows the relative differences, Pearson correlation and the FGE for PM_{10}. Over the Atlantic Ocean, the CRs concentrations are relatively close to the NR, except for the CR4 which overestimates the concentration of PM_{10}. All CRs present high concentrations of PM_{10} all over North Africa. This corresponds to high emissions of desert dust over this area,
25 which cause an important overestimation of PM_{10} compared to the NR. This overestimation can also be observed around all the Mediterranean Basin. The CRs tend to overestimate the PM_{10} concentrations over Spain, Italy, the Alps, Greece, Turkey, the north of the UK, the Iceland and the Norway. The overestimation over the Alps, Iceland and Norway are located at places of negligible concentrations. Over the rest of the European continent, CRs underestimate the concentration of PM_{10}, slightly for CR1, but very pronounced for CR2, CR3 and CR4. The area where the consistency between the CRs and the NR
30 is better is the Atlantic Ocean with a correlation ranging from 0.6 to 0.9 and a low FGE around 0.3. Over the Mediterranean Basin the correlation varies significantly between 0 and 1. Low correlations correspond to high FGE around 1. Over the continent, the correlation varies from 0.4 to 0.9 following a west-east axis. The correlations are slightly greater for CR1 than for the other CRs. The FGE over the continent changes significantly between the CR1 and the other CRs, respectively around 0.35 and 0.55. Similar conclusions can be obtained for the $PM_{2.5}$ comparison (see complementary materials). A

11

similar comparison has been done for the AOD between the CRs simulations and the NR simulation (see complementary materials).

In summary, the control runs present spatial variability along with temporal variability. The closest CR to the NR is the CR1. In terms of surface concentrations in PM, the CR3 is the most distant, while in terms of AOD the CR4 is the most distant. Those differences and the use of different CRs, coupled with the realism of the NR, demonstrate the robustness of the OSSE to evaluate the added value provided by AOD derived from the FCI.

5 Assimilation of FCI synthetic observations

The purpose of this paper is to assess the potential contribution of FCI VIS04 channel to the assimilation of aerosols on a continental scale. In our OSSE, MOCAGE represents the atmosphere with a horizontal resolution of 0.2 ° (around 20 km at the equator). Synthetic observations are therefore computed at the model resolution although FCI scans around 1 km resolution at the equator and 2 km over Europe. To fit with the timestep of our assimilation cycle, synthetic observations are also created every hour, although the future FCI imager could retrieve radiance observations every 10 minutes over the globe, and 2.5 minutes over Europe with the European Regional-Rapid-Scan. This means that for each profile of our simulation, only one synthetic observation is available each hour, instead of 24x10x10 at best (FCI scans 24 times an hour, with a spatial resolution 10 times higher than the model over the Europe). The use of one observation for each profile in an assimilation window is due to the assimilation system design that does not allow multiple observations for a same profile. In practice, future FCI observations could be averaged over each MOCAGE profile to reduce the impact of the instrument errors on assimilated observations.

The 3D-FGAT assimilation scheme integrates the synthetic observations described in Sect. 3. Before assimilation, a thinning process is applied to the synthetic observations to keep spatially only 1 pixel out of 4. Such thinning is useful to reduce the computation time, by accelerating the convergence of the cost function (not shown). The spatial correlation length of the B background covariance matrix is set to 0.4° in order to have a spatial impact of the assimilation on the simulation while not having multiple coverage of assimilated observations over one profile. The result of this thinning procedure changes only slightly the assimilated fields but saves significantly computing time. Assimilation simulations (ARs) are run for all CRs simulations using the same generated set of synthetic observations over the period of 4 months, from the 1st of January to the 30th of April. The standard deviation of errors used for B and R matrix are estimated respectively at 24 % and 12 %, as in Sič et al. (2016).

To assess the impact of the assimilation of FCI synthetic AOD observations, the CR forecasts and the AR analyses are compared to the assimilated synthetic observations. Figure 10 shows the histograms of the differences between the synthetic observations and the forecast field (in blue) and between synthetic observations and analyzed fields (in purple) for the four ARs simulations. The histograms follow a Gaussian shape, and the distribution of the analyzed values are closer to the synthetic observations than the forecast values. The spread of the histograms is smaller for the analyzed fields than for the

forecast fields. The assimilation of synthetic AODs hence improved the representation of AOD fields in the assimilation simulations. Besides, the spatial comparisons between the simulations and the NR show improvements in the AOD fields of simulations by assimilation of the synthetic observations (see supplementary material Fig. S5, S6, S7 and S8). As the increment is applied to all aerosol bins and that PM_{10} corresponds to 5 of the 6 bins while $PM_{2.5}$ to only 4, we expect better

5   corrections for PM_{10} concentrations than for $PM_{2.5}$ concentrations.

To validate the results of the OSSEs, the simulations are compared to the reference simulation (NR) over the period. Figure 11 exhibits the spatial differences in surface concentrations of PM_{10} between the ARs and the NR. It shows the mean relative bias, the correlation and the FGE for every simulations. Using Fig. 9 as a reference, the relative bias, the FGE and the correlation have been improved over most parts of the domain after assimilation for all simulations. Over the European

10   continent, all simulations show a strong improvement of the statistical indicators. For instance in CR3, along a line that goes from Spain to Poland, the FGE decreases by about 0.1 after assimilation, In the Eastern part of Europe (from the Turkey to Finland), the decrease of FGE is even higher. Over North Africa and the Mediterranean Sea the improvement is intermediate. Nevertheless, the mean bias over the ocean tends to increase for the simulations, especially for AR4. This can also be observed for the $PM_{2.5}$ concentration comparison (see supplementary material S1, S2, S3 and S4).

15   The assimilation of the synthetic observations has a positive impact at each layer of the model. The mean vertical concentrations of PM_{10} and $PM_{2.5}$ of the different simulations are respectively represented in Fig. 12 and 13, from the surface (level 47) up to 6 km (level 30). The positive impact along the vertical of the assimilation of AOD in the CTM MOCAGE is due to the use of the vertical representation of the model to distribute the increment. Sič et al (2016) showed that the assumption of using the vertical representation of the model gives good assimilation results with the regular MOCAGE setup

20   that distributes emissions over the 5 lowest vertical levels. However, the performance of the assimilation may depend on the realism of the representation of aerosols along the vertical in the CTM. The CRs simulations, in red, overestimate the PM_{10} concentrations of the NR, in purple, due to the overestimation of desert dust concentrations in the CRs simulations. This overestimation is not present in the $PM_{2.5}$ concentrations because this is the fraction of aerosols where there are few desert dusts. For the first three simulations, the vertical PM_{10} concentrations are well corrected by the assimilation, while for

25   simulation 4, the correction is less relevant for the levels near the surface. The assimilation tends to decrease the $PM_{2.5}$ concentrations above the level 42 and to increase the concentrations under that level. Simulation 4 presents a decay of the surface concentrations of $PM_{2.5}$. The correction of concentrations is more pertinent for the PM_{10} concentrations than for the $PM_{2.5}$ concentrations, which was expected.

The vertical distribution of aerosol concentrations between the CR4 simulations and the NR explains why the bias over the

30   ocean tends to increase. At the lowest level, the concentration of PM_{10} is more important, since the CR4 emits only at the surface level, while the AOD is less important, since the aerosol loss by dry deposition increases. The positive increment is therefore added preferentially to the surface level, which increases the bias at surface.

13

To evaluate the capability of the FCI 444 nm channel observations to improve aerosol forecast in an air quality scenario, the ARs simulations have been compared to the NR using the synthetic AQeR stations as in Sect. 4. Tables 7 and 8 show the statistics of the comparison between the ARs and the NR for PM_{10} and $PM_{2.5}$ concentrations. With regard of the comparison of the CRs against the NR in Tab. 5 and 6, the ARs are more consistent with the NR. The bias is reduced for both PM_{10} and

5    $PM_{2.5}$ concentrations. The RMSE and the FGE decrease while the Factor of 2 and the correlations increase for all ARs compared to their respective CRs.

The daily medians of PM_{10} and $PM_{2.5}$ concentrations at all stations are represented over time in Fig. 14 and 15 for the four simulations. The assimilation reduces the gap between the simulations and the NR over the entire period. Around the secondary inorganic aerosol episode, 65th day of simulation, the improvements of PM_{10} and $PM_{2.5}$ surface concentrations are

10   significant for simulations 2, 3 and 4.

From an air quality monitoring perspective, the assimilation of the FCI synthetic AOD at 444 nm in MOCAGE improves strongly the surface PM_{10} concentrations in the 4 simulations over the European continent for the period January-April 2014. To quantify the improvement of simulations through the assimilation of FCI synthetic observations during a severe pollution episode for (7th-15th March) over Europe, maps of relative concentrations of PM_{10} and FGE are respectively represented for

15   the CRs comparison and for the ARs comparison in Fig. 16 and 17. The simulations CR2, CR3 and CR4 underestimate PM_{10} concentrations for 70 % over all Europe compared to the NR. The FGE presents high values going from 0.55 to 0.85. The assimilation of synthetic AOD improves meaningfully the surface concentrations of aerosols over the continent in the simulations, but the simulations still underestimate the PM_{10} concentrations by 30-20 %. Important changes in the FGE are noticeable, with values dropping from 0.55-0.85 down to 0.2-0.4 for all simulations. Over the other areas, the assimilation

20   reduces significantly the relative bias and the FGE. Thus, the assimilation of synthetic observations improves significantly the representation of the surface PM_{10} concentrations of simulations during the pollution episode.

In summary, the use of synthetic observations at 444 nm of the future sensor FCI through assimilation improves significantly the aerosol fields of the simulations over the European domain from January to April 2014. These improvements are located

25   all over the domain with best results over the European continent and the Mediterranean area. The improvement of the vertical profile of aerosol concentrations is also noticeable, and it may be explained because different parts of the column can be transported by winds in different directions (Sič et al, 2016), although the AOD synthetic observations do not provide information along the vertical. The first two simulations give better results over the ocean than simulations 3 and 4, due to a closer representation of the vertical profile of the aerosol concentrations. This may show an overly optimistic aspect of the

30   OSSE of the first two simulations. The simulations lead to sufficiently reliable results since the shapes of their vertical profile of aerosol concentrations are different from those of the NR. These differences are caused by the way emissions are injected in the atmosphere (higher for simulation 3 and lower for simulation 4). The simulations 3 and 4 present robust results over continent, despite the differences in the vertical representation of aerosol concentrations.

6 Discussion

Although the results have shown a general benefit of FCI/VIS04 future measurements for assimilation in the CTM MOCAGE, some limitations must be addressed. The AOD does not introduce information on the vertical distribution of PM, nor on the size distribution and type of aerosols. So, the performance of the assimilation will largely depend on the realism of the representation of aerosols in the CTM before assimilation. If, for instance, the model has a positive bias in AOD and a negative bias in surface PM10 compared to observations, then the assimilation could lead to detrimental results. So the AOD and PM biases should be assessed and corrected as far as possible, before assimilation, in order to avoid detrimental assimilation.

To identify the added value of assimilating FCI/VIS04 AOD, it is needed to compare the results with the assimilation of present-day observations, such as imagers on LEO satellites and in-situ surface PM observations. The assimilation of PM surface observations is indeed an efficient way to improve PM concentration fields at surface (Tombette et al, 2009), but the correction of the fields remains confined to the lowermost levels. While improving the PM surface fields, it has been shown that the assimilation of AOD also gives a better representation of aerosols along the vertical (Fig. 12 and 13) and of the AOD fields, which are important added value that the assimilation of PM surface observations only cannot achieve. Besides, the satellite coverage is much broader than the coverage of in-situ network and, for instance, aerosol fields over the seas can be corrected before they reach the coast.

In order to assess the added-value of a high repetitivity measurements of FCI compared to a LEO satellite, a complementary experiment, called AR3LEO, has been done. This experiment is based on the CR3 configuration of MOCAGE, but the synthetic observations kept are only the ones at 12UTC, instead of the hourly observations. By taking into account only one measurement per pixel per day, AR3LEO should thus simulate the assimilation of a LEO satellite. The results of AR3LEO are in Tab. 9 and Fig. 18. The density of observations assimilated is about 10 times lower than the density of FCI assimilated data. Most of the scores (except the PM2.5 correlation) of AR3LEO are between the CR3 and the AR3 scores, which shows and quantifies the benefit of FCI compared to a LEO satellite. This is confirmed also on the time series of PM_{10} surface concentrations show (Fig. 18): the AR3LEO simulation is closer to the CR3 simulation than to the AR3 simulation. During the pollution episodes from 7 to 14 March 2014 (Fig. 18, time series between day 60 and day 67, and maps), the amplitude of PM concentrations is underestimated more in AR3LEO than in AR3. The maps of bias and FGE show better scores in AR3 than in AR3LEO at the locations where pollution occurs.

The results have shown the potential benefit of assimilating AOD data from the future FCI/VIS04 in a chemistry-transport model for monitoring the PM concentrations at regional scale over Europe. The horizontal and temporal resolution of FCI (2 km horizontal grid every 10 minutes or even 2.5 minutes in Regional Rapid Scan) will however be much finer than the regional scales that have been considered in this study: (0.2° horizontal grid every hour). The large differences between the resolution of future FCI data and the data used in this OSSE have two important implications that deserve to be presented. Firstly, in order to get closer to the future data, one could consider generating synthetic observations at the full FCI

resolution and assimilate them in a regional-scale assimilation system. The use of multiple observations using a "super-observation" approach, by spatial and temporal averaging, should reduce the instrumental errors and thus one may expect that the assimilation of real FCI data can lead to even better results than the OSSE presented here. Secondly, it is worth considering whether high-resolution FCI measurements could be assimilated in a high-resolution model for kilometre-scale monitoring of air quality. However, such work is presently limited by the present state of the art of numerical chemistry models and of their input emission data. The conclusions of some recent numerical experiments with kilometre-scale air quality models (Colette et al, 2014) are that such models are very expensive and that the emission inventories do not have a sufficient resolution. Still, the performance of such high resolution models are better than coarser resolution ones. As computing capacities keep increasing and kilometre-scale air quality models become affordable, it will be interesting to evaluate the benefit of assimilating high resolution FCI data in a kilometre-scale air quality model, even if the emission data is built with coarse assumptions. One might expect that the assimilation of FCI data could correct enough the model state to balance the deficiencies of the emission inventories. For such study, high temporal repetitivity may be also of high interest.

7 Conclusion

An OSSE method has been developed to quantify the added value of assimilating future MTG/FCI VIS04 AOD (444 nm) for regional-scale aerosol monitoring in Europe.. The characteristic errors of the FCI have been computed from a sensitivity analysis and introduced in the computation of synthetic observations from the NR. An evaluation of the realistic state of the atmosphere of the NR has been done, as well as a comparison of CR simulations with the NR, in order to avoid the identical twin problem mentioned in Timmermans et al. (2009a). Furthermore, different control run simulations have been set up as in Claeyman et al. (2011) to avoid this issue. The results of the OSSE should hence be representative of the results that the assimilation of real retrieved AODs from the FCI sensor will bring.

Although the use of a single synthetic observation per profile and the choice of an albedo error of 10% are pessimistic choices, the assimilation of synthetic AOD at 444 nm showed a positive impact, particularly for the European continental air pollution. The simulations with data assimilation reproduced spatial and temporal patterns of PM_{10} concentrations at surface better than without assimilation all along the simulations and especially during the high pollution event of March. The improvement of analysed fields is also expected for other strong pollution event such as a volcanic ash plume. This capability of synthetic observations to improve the analysis of aerosols is present for the 4 set of simulations which show the capability of future data from the FCI sensor to bring an added value within the CTM MOCAGE aerosol forecasts, and in general, in atmospheric composition models. Moreover, the advantage of a GEO platform over a LEO satellite has been shown and assessed.

The results over ocean show an increase of PM concentration bias after assimilation in some places, particularly for AR4. An explanation is that AOD does not introduce information vertically and that the correction of aerosols in the vertical relies on

16

the model vertical distribution. For a satisfactory assimilation of AOD, the AOD and PM biases of the model should be assessed and corrected as far as possible. Another perspective is to use multiple wavelengths, using the Ångström exponent, could avoid this problem by better distributing the increment of AOD between the different bins and hence the different species. Sič et al. (2016) also recommended the use of other types of observations, such as lidars, in the assimilation process to introduce information over the vertical.

The results presented here in this OSSE are encouraging for the use of future FCI AOD data within CTMs for the wavelength VIS04 centered at 444 nm. The use of other channels could bring complementary information, such as the NIR2.2 that is expected to be less sensitive to fine aerosols but more sensitive to large aerosols such as desert dusts and sea salt aerosols. Future work may also consider exploiting the high-resolution of FCI, following two possible lines: either for regional-scale assimilation by using a "super-observation" procedure, or for kilometre-scale air quality mapping and for assessing the quality of emission inventories. However, such extension is mostly depending on improvements in the numerical chemistry models, in the input emission data and in the optimization of assimilation algorithms.

Appendix: Deriving AOD error variance from the Global Sensivitiy Analysis of FCI/VIS04 reflectance

The general method is summarized in Figure A1. A sensitivity analysis has been performed for each OPAC aerosol types, using Monte-Carlo FCI simulations of about 200.000 draws in the prior distribution of the input parameters. The input distribution of AOD and of total ozone and water vapor columns are obtained from a MOCAGE simulation ran over the whole 2013 year. The distribution of ground albedo is deduced from the OPAC database. The profiles of the MOCAGE simulation are classified into OPAC (Hess et al., 1998) types by making correspondence between species as Ceamanos et al. (2014) and then by applying classification criteria similar to the OPAC types.

For every OPAC type, a global sensitivity analysis (GSA) has been performed between the input (AOD τ, total column water vapour, ozone content), ground albedo ρ_g and solar zenithal angle θ_S) distributions and the output (VIS04 reflectance) distributions of the FCI simulator. Under the assumption of independent inputs, the Sobol (1990, 1993) indices enable a ranking of inputs or couple of inputs with respect their variance-based importance in the total output variance. For VIS04, the variability of the solar zenithal angle, the ground albedo and the AOD are the three largest Sobol indices in that order and, together, they are at the origin of more than 98 % of the total variance of the output reflectance. Following Sobol (1996), the GSA can also be used to determine a truncated version of the Hoeffding (1948, ANOVA) functional decomposition, with key inputs, that approximates the analyzed reflectance. For all OPAC groups, the dependence of

17

reflectance for VIS04 on the total ozone column and water vapor is negligible and is not taken into account in the reflectance approximation. As a consequence, the reflectance R can be approximated by the following equation:

$$R = f_3(\theta_S) + f_2(\rho_g) + f_1(\tau) + \epsilon, \tag{2}$$

where f_1, f_2, and f_3 are functions of the solar zenithal angle, the ground albedo and the AOD, respectively. The approximation error ϵ, exhibits a root mean square (RMS) less than 0.7 W m^{-2} sr^{-1} µm^{-1} (1.5 % of the mean radiance values of 47.3 W m^{-2} sr^{-1} µm^{-1}).

As a consequence of this sensitivity analysis, it is then possible to isolate the AOD τ with respect the measured reflectance R, the other key inputs θ_S, ρ_g and the approximation error ϵ:

$$\tau = F(R, \theta_S, \rho_g, \epsilon). \tag{3}$$

By sampling input distributions on this equation (Monte-Carlo method), the root mean square error (RMSE) of the AOD retrieval can be derived as a function of the reflectance R, the solar zenithal angle θ_S the ground albedo ρ_g, and of their uncertainty. R is associated with a measurement noise. No uncertainty is prescribed for the solar zenithal angle. For a given fixed value of relative error of ground albedo, a look-up-table is built, that provides the root mean square error (RMSE) of the AOD retrieval as a function of the solar zenithal angle and of the ground albedo. Such a look-up-table of the RMSE of VIS04 AOD has been computed for every OPAC types and for different possible values of surface albedo errors.

References

Alfaro, S. C., Gaudichet, A., Gomes, L., and Maillé, M.: Mineral aerosol production by wind erosion: aerosol particle sizes and binding energies, Geophys. Res. Lett., 25, 991–994, 1998.

Aoun, Y.: Evaluation de la sensibilité de l'instrument FCI à bord du nouveau satellite Meteosat Troisième Génération imageur (MTG-I) aux variations de la quantité d'aérosols d'origine désertique dans l'atmosphère. Thèse de Doctorat PSL Research University, 2016.

Aoun, Y., Blanc, P., Wald, L., Mathieu, S., and Claeyman, M.: The use of global sensitivity analysis for assessing capability of the MTG/FCI instrument to detect aerosols. In Proceedings of the 2015 EUMETSAT Meteorological Satellite Conference, Toulouse, France, 21-25 Sep 2015. http://www.eumetsat.int/website/home/News/ConferencesandEvents/DAT_2305526.html (session 3), Aoun.pdf, 2015.

Bäumer, D., Vogel, B., Versick, S., Rinke, R., Möhler, O., and Schnaiter, M.: Relationship of visibility, aerosol optical thickness and aerosol size distribution in an ageing air mass over South-West Germany, Atmos. Environ., 42, 989–998, 2008.

Bechtold, P., Bazile, E., Guichard, F., Mascart, P., and Richard, E.: A mass-flux convection scheme for regional and global models, Q. J. Roy. Meteor. Soc., 127, 869–886, 2001.

Benedetti, A., Morcrette, J.-J., Boucher, O., Dethof, A., Engelen, R., Fisher, M., Flentje, H., Huneeus, N., Jones, L., Kaiser, J., et al.: Aerosol analysis and forecast in the European centre for medium-range weather forecasts integrated forecast system: 2. Data assimilation, J. Geophys. Res. - Atmos., 114, 2009.

Bernard, E., Moulin, C., Ramon, D., Jolivet, D., Riedi, J., and Nicolas, J.-M.: Description and validation of an AOT product over land at the 0.6 [mu] m channel of the SEVIRI sensor onboard MSG, Atmos. Meas. Tech., 4, 2543, 2011.

Brook, R. D., Franklin, B., Cascio, W., Hong, Y., Howard, G., Lipsett, M., Luepker, R., Mittleman, M., Samet, J., Smith, S. C., et al.: Air pollution and cardiovascular disease, Circulation, 109, 2655–2671, 2004.

Carrer, D., Roujean, J.-L., Hautecoeur, O., and Elias, T.: Daily estimates of aerosol optical thickness over land surface based on a directional and temporal analysis of SEVIRI MSG visible observations, J. Geophys. Res. - Atmos., 115, 2010.

Castro, L., Pio, C., Harrison, R. M., and Smith, D.: Carbonaceous aerosol in urban and rural European atmospheres: estimation of secondary organic carbon concentrations, Atmos. Environ., 33, 2771–2781, 1999.

Ceamanos, X., Carrer, D. and Roujean, J.L.: Improved retrieval of direct and diffuse downwelling surface shortwave flux in cloudless atmosphere using dynamic estimates of aerosol content and type: Application to the LSA-SAF project. Atmos. Chem. Phys.,15 ,8209-8232, 2014.

Claeyman, M., Attié, J.-L., Peuch, V.-H., El Amraoui, L., Lahoz, W. A., Josse, B., Joly, M., Barré, J., Ricaud, P., Massart, S., et al.: A thermal infrared instrument onboard a geostationary platform for CO and O3 measurements in the lowermost troposphere: Observing System Simulation Experiments (OSSE), Atmos. Meas. Tech., 4, 1637, 2011.

Colette, A., B. Bessagnet, F. Meleux, E. Terrenoire, and L. Rouïl,: Frontiers in air quality modelling. Geosci. Model Dev., 7, 203-210, 2014.

Curci, G., C. Hogrefe, R. Bianconi, U. Im, A. Balzani, R. Baro, D. Brunner, R. Forkel, L. Giordano, M. Hirtl: Uncertainties of simulated optical properties induced by assumption on aerosol physical and chemical properties: an AQMEII-2 perspective, Atmos. Environ., 115, 541-552, 2015.

Dufour, A., Amodei, M., Ancellet, G., and Peuch, V.-H.: Observed and modelled "chemical weather" during ESCOMPTE, Atmos. Res., 74, 161–189, 2005.

EEA: Air quality in Europe — 2014 report, https://www.eea.europa.eu/publications/air-quality-in-europe-2014/.

Edwards, D. P., A. .F. Arellano Jr., M. N., and M. N. Deter, A satellite observation system simulation experiment for carbon monoxide in the lowermost atmosphere, J. Geophys. Res., 114, D14304, 2009.

Eskes, H., Huijnen, V., Arola, A., Benedictow, A., Blechschmidt, A., Botek, E., Boucher, O., Bouarar, I., Chabrillat, S., Cuevas, E., et al.: Validation of reactive gases and aerosols in the MACC global analysis and forecast system, Geosci. Model. Dev., 8, 3523, 2015.

Eumetsat: URD Eumetsat, http://www.eumetsat.int/website/wcm/idc/idcplg?IdcService=GET_FILE&dDocName=pdf_mtg_eurd& RevisionSelectionMethod=LatestReleased&Rendition=Web, 2010.

19

Fountoukis, C. and Nenes, A.: ISORROPIA II: a computationally efficient thermodynamic equilibrium model for K+–Ca 2+–Mg 2+–NH4+–Na+–SO 4 2—NO 3—Cl—H 2 O aerosols, Atmos. Chem. and Phys., 7, 4639–4659, 2007.

Gerber, H. E.: Relative-humidity parameterization of the Navy Aerosol Model (NAM), Tech. rep., NAVAL RESEARCH LAB WASHINGTON DC, 1985.

5 Gong, S.: A parameterization of sea-salt aerosol source function for sub-and super-micron particles, Global Biogeochem. Cy., 17, 2003.

Granier, C., Bessagnet, B., Bond, T., D'Angiola, A., van Der Gon, H. D., Frost, G. J., Heil, A., Kaiser, J. W., Kinne, S., Klimont, Z., et al.: Evolution of anthropogenic and biomass burning emissions of air pollutants at global and regional scales during the 1980–2010 period, Climatic Change, 109, 163, 2011.

10 Guffanti, M., Casadevall, T. J., and Budding, K. E.: Encounters of aircraft with volcanic ash clouds: a compilation of known incidents, 1953-2009, US Department of Interior, US Geological Survey, 2010.

Guth, J., Josse, B., Marécal, V., Joly, M., and Hamer, P. D.: First implementation of secondary inorganic aerosols in the MOCAGE version R2. 15.0 chemistry transport model, Geosci. Model. Dev., 9, 137-160, 2016.

Hess, M., Koepke, P., and Schult, I.: Optical properties of aerosols and clouds: The software package OPAC, B. Am. M
15 eteorol. Soc., 79, 831–844, 1998.

Hoeffding, W.: A class of statistics with asymptotically normal distribution, Ann. Math. Stat., pp. 293–325, 1948.

Holben, B. N., Eck, T., Slutsker, I., Tanre, D., Buis, J., Setzer, A., Vermote, E., Reagan, J., Kaufman, Y., Nakajima, T., et al.: AERONET—A federated instrument network and data archive for aerosol characterization, Remote Sens. Environ., 66, 1–16, 1998.

20 Im, U., Bianconi, R., Solazzo, E., Kioutsioukis, I., Badia, A., Balzarini, A., Baró, R., Bellasio, R., Brunner, D., Chemel, C., et al.: Evaluation of operational on-line-coupled regional air quality models over Europe and North America in the context of AQMEII phase 2. Part I: Ozone, Atmos. Environ., 115, 404–420, 2015.

Jaeglé, L., Quinn, P., Bates, T., Alexander, B., and Lin, J.-T.: Global distribution of sea salt aerosols: new constraints from in situ and remote sensing observations, Atmos. Chem. Phys., 11, 3137–3157, 2011.

25 Joly, M. and Peuch, V.-H.: Objective classification of air quality monitoring sites over Europe, Atmos. Environ., 47, 111–123, 2012.

Josse, B.: Représentation des processus de transport et de lessivage pour la modélisation de la composition chimique de l'atmosphère à l'échelle planétaire, Ph.D. thesis, Toulouse 3, 2004.

Kaiser, J., Heil, A., Andreae, M., Benedetti, A., Chubarova, N., Jones, L., Morcrette, J.-J., Razinger, M., Schultz, M., Suttie,
30 M., et al.: Biomass burning emissions estimated with a global fire assimilation system based on observed fire radiative power, Biogeosciences, 9, 527, 2012.

Kirchstetter, T. W., Novakov, T., and Hobbs, P. V.: Evidence that the spectral dependence of light absorption by aerosols is affected by organic carbon, J. Geophys. Res. - Atmos., 109, 2004.

Koepke, P., Hess, M., Schult, I., and Shettle, E.: Global aerosol data set, MPI Meteorologie Hamburg Rep, 243, 44, 1997.

Kuenen, J., Visschedijk, A., Jozwicka, M., and Denier Van Der Gon, H.: TNO-MACC_II emission inventory; a multi-year (2003–2009) consistent high-resolution European emission inventory for air quality modelling, Atmos. Chem. Phys., 14, 10 963–10 976, 2014.

IPCC: Climate change 2007-the physical science basis: Working group I contribution to the fourth assessment report of the IPCC, vol. 4, Cambridge University Press, 2007.

Lahoz, W. A., V.-H. Peuch, J. Orphal, J.-L. Attié, K. Chance, X. Liu, D. Edwards, H. Elbern, J.-M. Flaud, M. Claeyman, L. El Amraoui, Monitoring air quality from space: the case of geostationary platform, Bull. Am. Meteorol. Soc., 93, 221-233, 2012.

Lamarque, J.-F., Bond, T. C., Eyring, V., Granier, C., Heil, A., Klimont, Z., Lee, D., Liousse, C., Mieville, A., Owen, B., et al.: Historical (1850–2000) gridded anthropogenic and biomass burning emissions of reactive gases and aerosols: methodology and application, Atmos. Chem. Phys., 10, 7017–7039, 2010.

Levy, R., Mattoo, S., Munchak, L., Remer, L., Sayer, A., Patadia, F., and Hsu, N.: The Collection 6 MODIS aerosol products over land and ocean, Atmos. Meas. Tech., 6, 2989, 2013.

Louis, J.-F.: A parametric model of vertical eddy fluxes in the atmosphere, Bound-Lay. Meteorol. 17, 187–202, 1979.

Marécal, V., Peuch, V.-H., Andersson, C., Andersson, S., Arteta, J., Beekmann, M., Benedictow, A., Bergström, R., Bessagnet, B., Cansado, A., et al.: A regional air quality forecasting system over Europe: the MACC-II daily ensemble production, Geosci. Model Dev., 8, 2777, 2015.

Martet, M., Peuch, V.-H., Laurent, B., Marticorena, B., and Bergametti, G.: Evaluation of long-range transport and deposition of desert dust with the CTM MOCAGE, Tellus B, 61, 449–463, 2009.

Marticorena, B. and Bergametti, G.: Modeling the atmospheric dust cycle: 1. Design of a soil-derived dust emission scheme, Journal of Geophysical Research: Atmospheres, 100, 16 415–16 430, 1995.

Massart, S., Clerbaux, C., Cariolle, D., Piacentini, A., Turquety, S., and Hadji-Lazaro, J.: First steps towards the assimilation of IASI ozone data into the MOCAGE-PALM system, Atmos. Chem. Phys., 9, 5073–5091, 2009.

Masutani, M., T. W. Schlatter, R. M. Errico, A. Stoffelen, E. Andersson, W. Lahoz, J. S. Woollen, G. D. Emmitt, L.-P. Riishøjgaard, and S. J. Lord: Observing system simulation experiments, Data Assimilation, 647-679, 2010.

Mayer, B. and Kylling, A.: The libRadtran software package for radiative transfer calculations-description and examples of use, Atmospheric Chemistry and Physics, 5, 1855–1877, 2005.

Mei, L., Xue, Y., Leeuw, G. d., Holzer-Popp, T., Guang, J., Li, Y., Yang, L., Xu, H., Xu, X., Li, C., et al.: Retrieval of aerosol optical depth over land based on a time series technique using MSG/SEVIRI data, Atmos. Chem. Phys., 12, 9167–9185, 2012.

Petty, G. W.: A first course in atmospheric radiation, Sundog Pub, 2006.

Peuch, V.-H., and R. Engelen: Towards and operational GMES Atmosphere Monitoring Service, ECMWF Newsletter, 132, 20–25, 2012.

21

Prank, M., Sofiev, M., Tsyro, S., Hendriks, C., Semeena, V., Vazhappilly Francis, X., Butler, T., Denier van der Gon, H., Friedrich, R., Hendricks, J., et al.: Evaluation of the performance of four chemical transport models in predicting the aerosol chemical composition in Europe in 2005, Atmos. Chem. Phys., 16, 6041–6070, 2016.

Rouil, L., Honore, C., Bessagnet, B., Malherbe, L., Meleux, F., Vautard, R., Beekmann, M., Flaud, J.-M., Dufour, A., Martin, D., et al.: PREV'AIR: an operational forecasting and mapping system for air quality in Europe, B. Am. Meteorol. Soc., 90, 73–83, 2009.

Seinfeld J.H. and Pandis S.N.: Atmospheric Chemistry and Physics, 1326 pp. John Wiley, Hoboken, NJ, 1998.

Sič, B., El Amraoui, L., Marécal, V., Josse, B., Arteta, J., Guth, J.. and Hamer, P. D.: Modelling of primary aerosols in the chemical transport model MOCAGE: development and evaluation of aerosol physical parameterizations. Geosci. Model Dev., 8, 381, 2015.

Sič, B., Amraoui, L. E., Piacentini, A., Marécal, V., Emili, E., Cariolle, D., Prather, M., and Attié, J.-L.: Aerosol data assimilation in the chemical transport model MOCAGE during the TRAQA/ChArMEx campaign: aerosol optical depth, Atmos. Meas. Tech., 9, 5535–5554, 2016.

Sobol, I. M.: On sensitivity estimation for nonlinear mathematical models, Matematicheskoe modelirovanie, 2, 112–118, 1990.

Sobol, I. M.: Sensitivity estimates for nonlinear mathematical models, Mathematical modelling and computational experiments, 1, 407–414, 1993.

Sobol, I. M.: On freezing of unessential variables, Moscow University Mathematics Bulletin, 51, 60–62, 1996.

Stocker, T.: Climate change 2013: the physical science basis: Working Group I contribution to the Fifth assessment report of the Intergovernmental Panel on Climate Change, Cambridge University Press, 2014.

Timmermans, R. M., Schaap, M., Builtjes, P., Elbern, H., Siddans, R., Tjemkes, S., and Vautard, R.: An observing system simulation experiment (OSSE) for aerosol optical depth from satellites, Journal of Atmospheric and Oceanic Technology, 26, 2673–2682, 2009a.

Timmermans, R. M., A. J. Segers, P. J. Builtjes, R. Vautard, R. Siddans, H. Elbern, S. A. Tjemkes, M. Schaap, The added value of a proposed satellite imager for ground level particulate matter analyses and forecasts, IEEE-JSTARS. J. Sel. Top. Appl. Earth Obs. Remote Sens., 271-283, 2009b.

Timmermans, R. M., Lahoz, W. A., Attié, J. L., Peuch, V. H., Curier, R. L., Edwards, D. P., ... & Builtjes, P. J. H.: Observing system simulation experiments for air quality, Atmos. Environ., 115, 199-213, 2015.

Tombette, M., V. Mallet, and B. Sportisse: PM10 data assimilation over Europe with the optimal interpolation method, Atmos. Phys. Chem, 9, 57-70, 2009.

van der Werf, G. R., Randerson, J. T., Giglio, L., Collatz, G. J., Kasibhatla, P. S., and Arellano Jr, A. F.: Interannual variability in global biomass burning emissions from 1997 to 2004, Atmos. Chem. Phys., 6, 3423–3441, 2006.

Vidot, J. and Borbás, É: Land surface VIS/NIR BRDF atlas for RTTOV-11: model and validation against SEVIRI land SAF albedo product, Q. J. Roy. Meteorol. Soc., 140, 2186–2196, 2014.

22

Vieno, M., Heal, M., Twigg, M., MacKenzie, I., Braban, C., Lingard, J., Ritchie, S., Beck, R., Móring, A., Ots, R., et al.: The UK particulate matter air pollution episode of March–April 2014: more than Saharan dust, Environ. Res. Lett., 11, 044 004, 2016.

Williamson, D. L. and Rasch, P. J.: Two-dimensional semi-Lagrangian transport with shape-preserving interpolation, Mon. Wea. Rev., 117, 102–129, 1989.

Wiscombe, W. J.: Mie scattering calculations: advances in technique and fast, vector-speed computer codes, Atmospheric Analysis and Prediction Division, National Center for Atmospheric Research Boulder, CO, 1979, revised 1996.

Wiscombe, W. J.: Improved Mie scattering algorithms, Applied optics, 19, 1505–1509, 1980.

Yumimoto, K., Nagao, T., Kikuchi, M., Sekiyama, T., Murakami, H., Tanaka, T., Ogi, A., Irie, H., Khatri, P., Okumura, H., et al.: Aerosol data assimilation using data from Himawari-8, a next-generation geostationary meteorological satellite, Geophy. Res. Lett., 43, 5886–5894, 2016.

Zoogman, P., D. J. Jacob, K. Chance, H. M. Worden, D. P. Edwards, L. Zhang, Improved monitoring of surface ozone by joint assimilation of geostationary satellite observations of ozone and CO, Atmos. Environ., 84, 254-261, 2014.

Tables :

	Bias (µg/m3)	RMSE (µg/m3)	FGE	FactOf2	R_P	R_S
NR's PM_{10}	- 6.23 (~ - 35.1 %)	16.2	0.56	64.7 %	0.452	0.537
NR's $PM_{2.5}$	- 3.20 (~ - 24.7 %)	11.9	0.543	67.5 %	0.535	0.602

Table 1: Bias, RMSE, FGE, Factor of 2, Pearson correlation (Rp) and Spearman correlation (Rs) of the NR simulation taking as reference the AQeR observations for hourly PM_{10} and $PM_{2.5}$ concentrations from January to April 2014.

	Bias	MNMB	RMSE	FGE	R_P
NR	0.043	0.39	0.09	0.531	0.56

Table 2: Bias, MNMB, RMSE, FGE and Pearson correlation (Rp) between the NR simulation and AERONET station for daily 500 nm AOD from January to April 2014.

24

Aerosol types	Surface Concentration in $\mu g/m^3$	Main species	Surface proportion over the total PM_{10}
DO. & DC.	-	DD	
MC.	-	SS	SS > 85 %
MPO.	-	SS	SS < 85 %
MPC.	-	SS	SS < 85 %
CC.	0 – 17	IWS	
CA.	17 – 34	IWS	
CP.	34 – 75	IWS	
U.	> 75	IWS	

Table 3: Conditions for classifying the MOCAGE NR into the OPAC types. The first condition is the surface concentrations, the second is the main specie at the surface between Desert Dust (DD), Sea Salts (SS) and IWS (Insoluble, Water soluble, and Soot) and the third is a condition of the species over all the aerosols concentration. A species is described as a main species if its concentrations is above each other concentrations, for example DD is a main species if [DD]>[SS] & [DD]>[IWS].

	Forecasts	SOA	Repartition of emissions from level 1 (surface layer) up to the 5th level
NR	ARPEGE	Yes	52%; 26%; 13%; 6%; 3%
CR1	IFS	Yes	52%; 26%; 13%; 6%; 3%
CR2	IFS	No	52%; 26%; 13%; 6%; 3%
CR3	IFS	No	30%; 24%; 19%; 15%; 12%
CR4	IFS	No	100%; 0%; 0%; 0%; 0%

Table 4: Table of differences between the NR simulation and the CRs simulations.

Hourly PM10 CRs « stations » vs NR « stations »	Bias (µg/m3)	RMSE (µg/m3)	FGE	FactOf2	R_P	R_S
CR1	-1.3 (-8.2 %)	7.9	0.332	89.1 %	0.671	0.748
CR2	-4.5 (-35.2 %)	9.3	0.47	75.6 %	0.609	0.709
CR3	-4.8 (-38.1 %)	9.8	0.511	69.3 %	0.572	0.671
CR4	-2.9 (-20.5%)	8.7	0.412	81.9 %	0.623	0.712

Table 5: Bias, RMSE, FGE, Factor of 2, Pearson correlation (Rp) and Spearman correlation (Rs) of the CRs simulation taking as reference the NR simulations for hourly PM$_{10}$ concentrations from January to April 2014. The comparison is made at the same station location as for AQeR stations.

5

Hourly PM2.5 CRs « stations » vs NR « stations »	Bias (µg/m3)	RMSE (µg/m3)	FGE	FactOf2	R_P	R_S
CR1	-0.8(-6.24%)	5.9	0.307	91.1 %	0.732	0.776
CR2	-3.9 (-37.4%)	7.1	0.452	78.4 %	0.69	0.731
CR3	-4.4 (-42.6%)	7.6	0.505	70.6 %	0.644	0.695
CR4	-1.8 (-15.1%)	6.6	0.374	85.5 %	0.665	0.73

Table 6: Bias, RMSE, FGE, Factor of 2, Pearson correlation (Rp) and Spearman correlation (Rs) of the CRs simulation taking as reference the NR simulations for hourly PM$_{2.5}$ concentrations from January to April 2014. The comparison is made at the same station location as for AQeR stations.

10

26

Hourly PM10 CRs « stations » vs NR « stations »	Bias (µg/m3)	RMSE (µg/m3)	FGE	FactOf2	R_P	R_S
AR1	-1.17 (-7.21 %)	7.16	0.296	92.2 %	0.739	0.791
AR2	-2.91 (-21.3 %)	8.1	0.373	85.3 %	0.694	0.751
AR3	-3.53 (-26.2 %)	8.67	0.417	80.4 %	0.67	0.726
AR4	-0.756 (-5.31 %)	8.03	0.339	88.2 %	0.691	0.759

Table 7: Bias, RMSE, FGE, Factor of 2, Pearson correlation and Spearman correlation of the ARs simulation taking as reference the NR simulations for hourly PM$_{10}$ concentrations from January to April 2014. The comparison is made at the same station location as for AQeR stations.

Hourly PM2.5 ARs « stations » vs NR « stations »	Bias (µg/m3)	RMSE (µg/m3)	FGE	FactOf2	R_P	R_S
AR1	-0.395 (-3.15%)	5.61	0.284	92.7 %	0.755	0.806
AR2	-2.28 (-20.5 %)	6.31	0.364	86.6 %	0.703	0.766
AR3	-2.94 (-27.1 %)	6.86	0.416	80.9 %	0.669	0.732
AR4	0.109 (0.9 %)	6.56	0.328	89.4 %	0.699	0.765

Table 8: Bias, RMSE, FGE, Factor of 2, Pearson correlation and Spearman correlation of the ARs simulation taking as reference the NR simulations for hourly PM$_{2.5}$ concentrations from January to April 2014. The comparison is made at the same station location as for AQeR stations.

5

10

27

Hourly AR3LEO « stations » vs NR « stations »	Bias (µg/m3)	RMSE (µg/m3)	FGE	FactOf2	R_P	R_S
PM10	-4.47 (-35.1 %)	9.11	0 .462	75.6 %	0.656	0.717
PM2.5	-3.89 (-37 %)	7.14	0.457	76.5 %	0.681	0.731

Table 9: Bias, RMSE, FGE, Factor of 2, Pearson correlation and Spearman correlation of the AR3LEO simulation taking as reference the NR simulations for hourly PM10 and PM$_{2.5}$ concentrations from January to April 2014. The comparison is made at the same station location as for AQeR stations.

Figures :
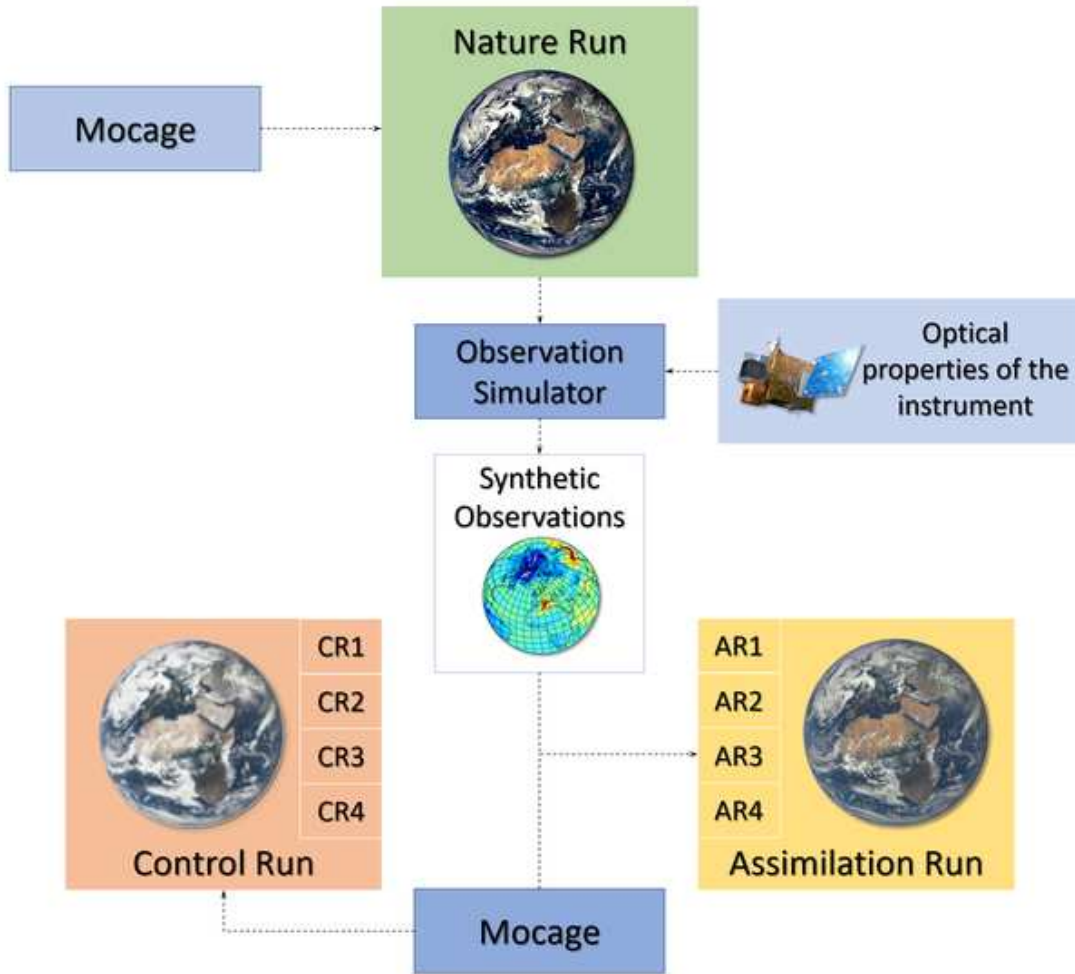
5   **Figure 1: Schematic representation of the OSSE principle.**
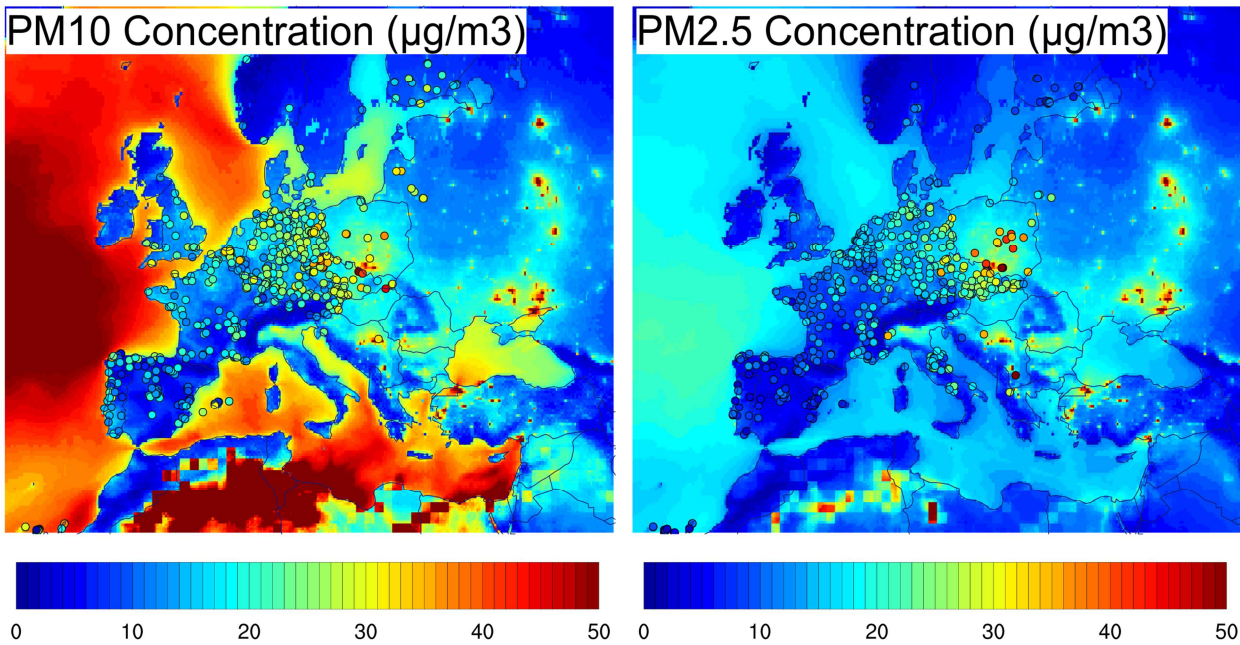
Figure 2: Mean PM$_{10}$ (left panel) and PM$_{2.5}$ (right panel) surface concentration (µg.m^{-3}) of the NR (shadings) and AQeR stations (color circles), from January to April 2014.

5
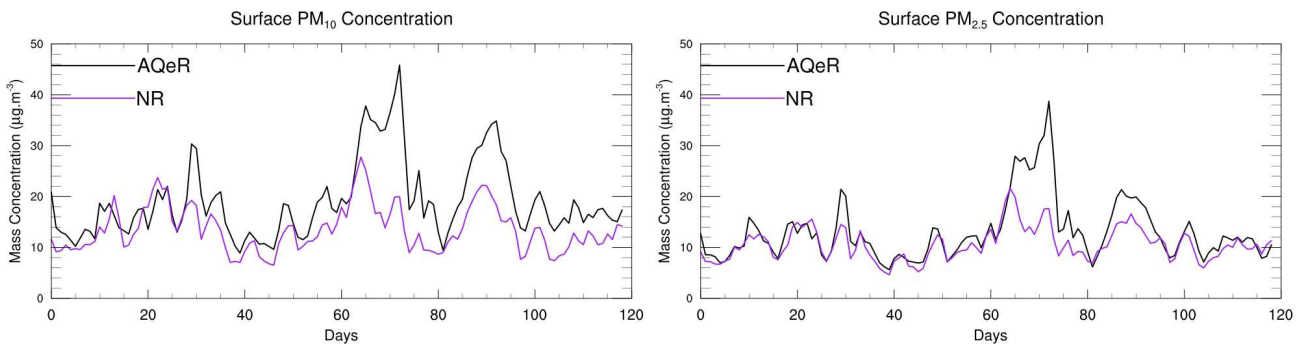
Figure 3: Median of the daily mean surface concentration in µg.m^{-3} of the NR (in purple) and the AQeR station (in black). The NR concentrations are calculated at the same locations as the AQeR stations, from 01/01/2014 (Day 1) until 30/04/2014 (last Day). The left panel is for PM$_{10}$ surface concentrations while the right one is for PM$_{2.5}$.

30
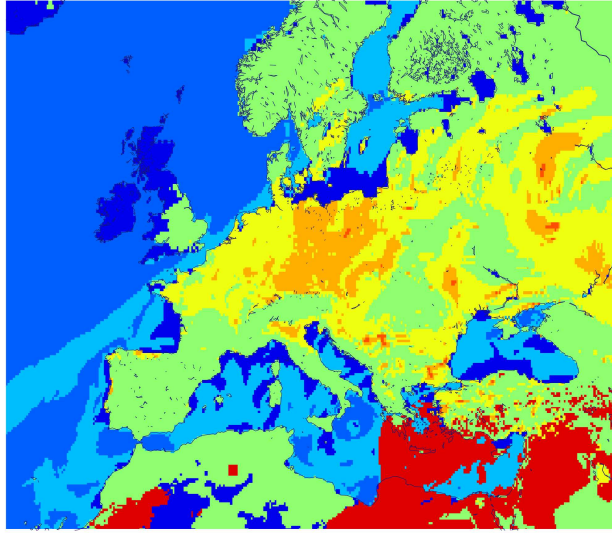
Figure 4: Classification of the NR profiles for the 7th of March 2014 at 12 UTC. Deep Blue is for dismissed profiles, Blue is for Maritime Clean, Light Blue for Maritime Polluted, Green is for Continental Clean, Yellow is for Continental Average, Orange is for Continental Polluted, Deep Orange is for Urban, and Red is for Desert Dust.

5

10

15

31
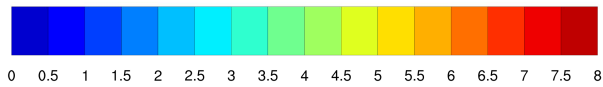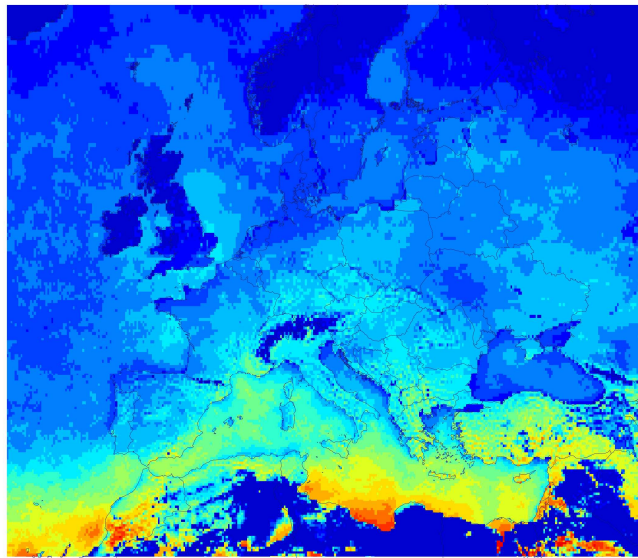
Figure 5: Average (from January to April) number of selected profiles per day, available for assimilation.
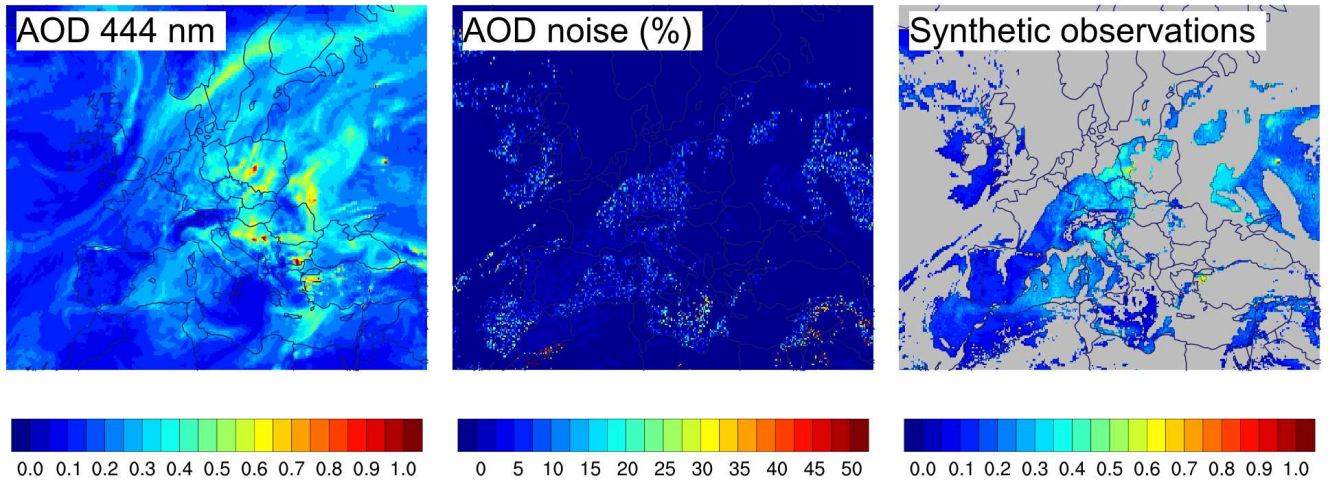
Figure 6: Example of generation of synthetic observations on the 7th of March 2014 at 12 UTC. From the NR's AOD as 444 nm (left panel), noise values representative of FCI (middle panel) are applied on every clear-sky pixel to generate the synthetic observations (right panel). The grey color represents the dismissed profiles.
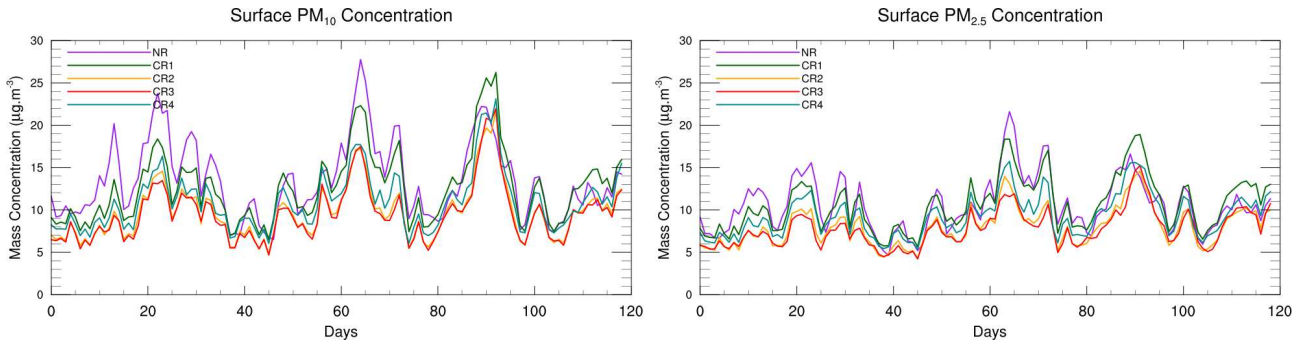
Figure 7: Median of the daily mean surface concentration of the NR (in purple) and the different CR (CR1 in green, CR2 in yellow, CR3 in red and CR4 in blue) determined for the same location as for the AQeR stations. The left graph is the PM$_{10}$ mass concentrations (µg.m^{-3}), while the right one represents the PM$_{2.5}$ mass concentrations.

5
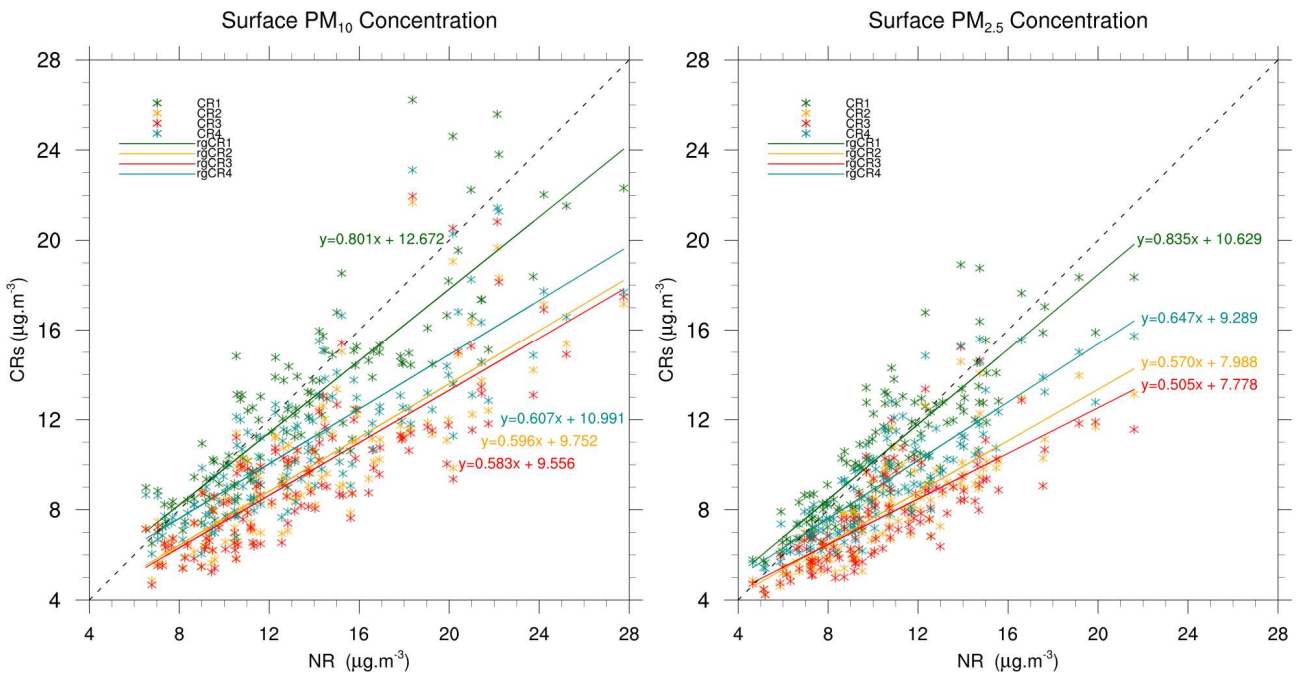
Figure 8: Scatter plot of the CRs daily surface concentrations (µg.m^{-3}) as function of NR daily surface concentrations for PM$_{10}$ (left) and PM$_{2.5}$ (right), for virtual stations and from January to April 2014. rgCRX are the linear regressions of each dataset.

33
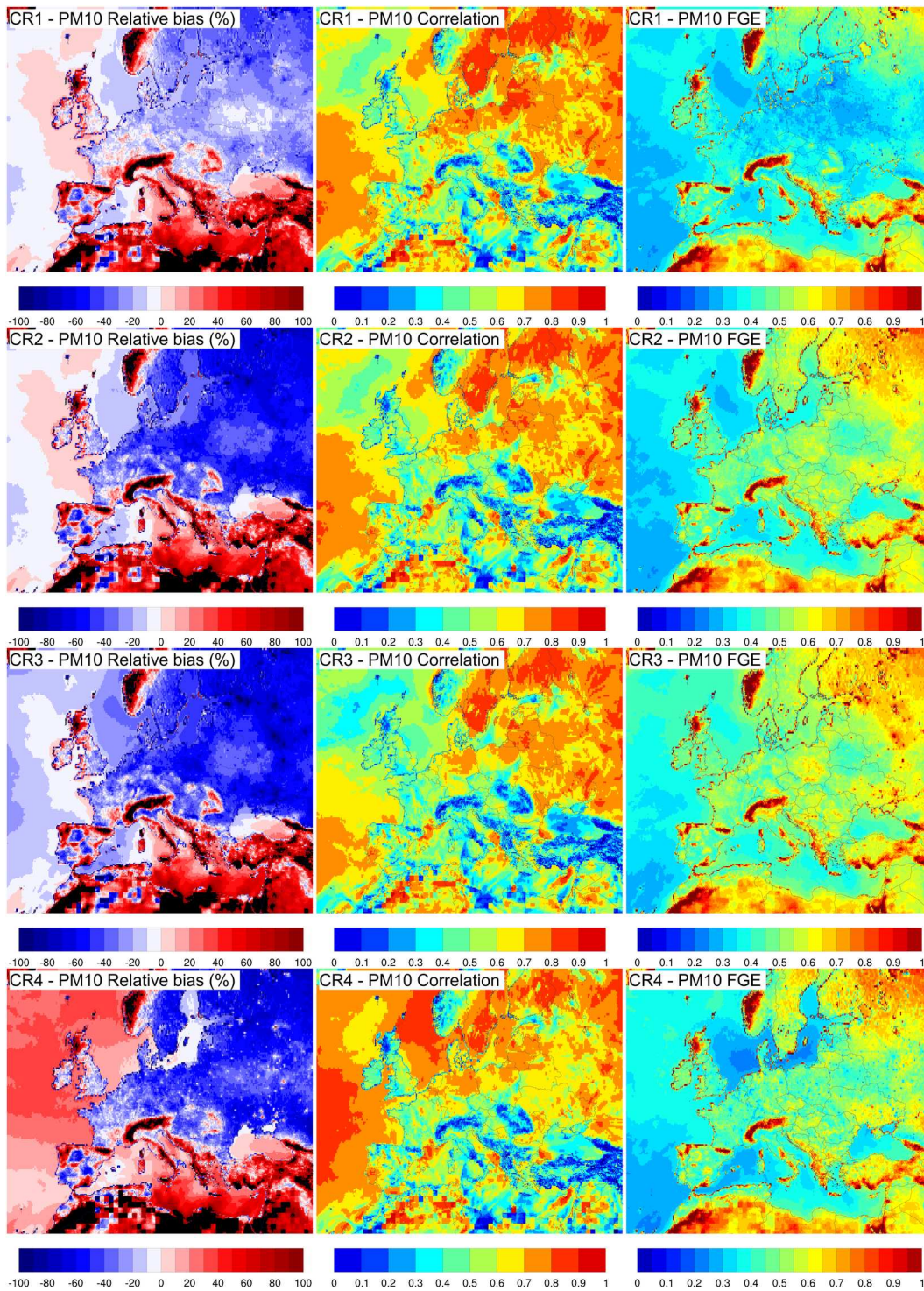
Figure 9: For each CR (CR1, CR2, CR3 and CR4), the figures represent a PM$_{10}$ comparison between the NR and the CRs from January to April 2014: the relative bias (in %), the Pearson correlation and the fractional gross error.
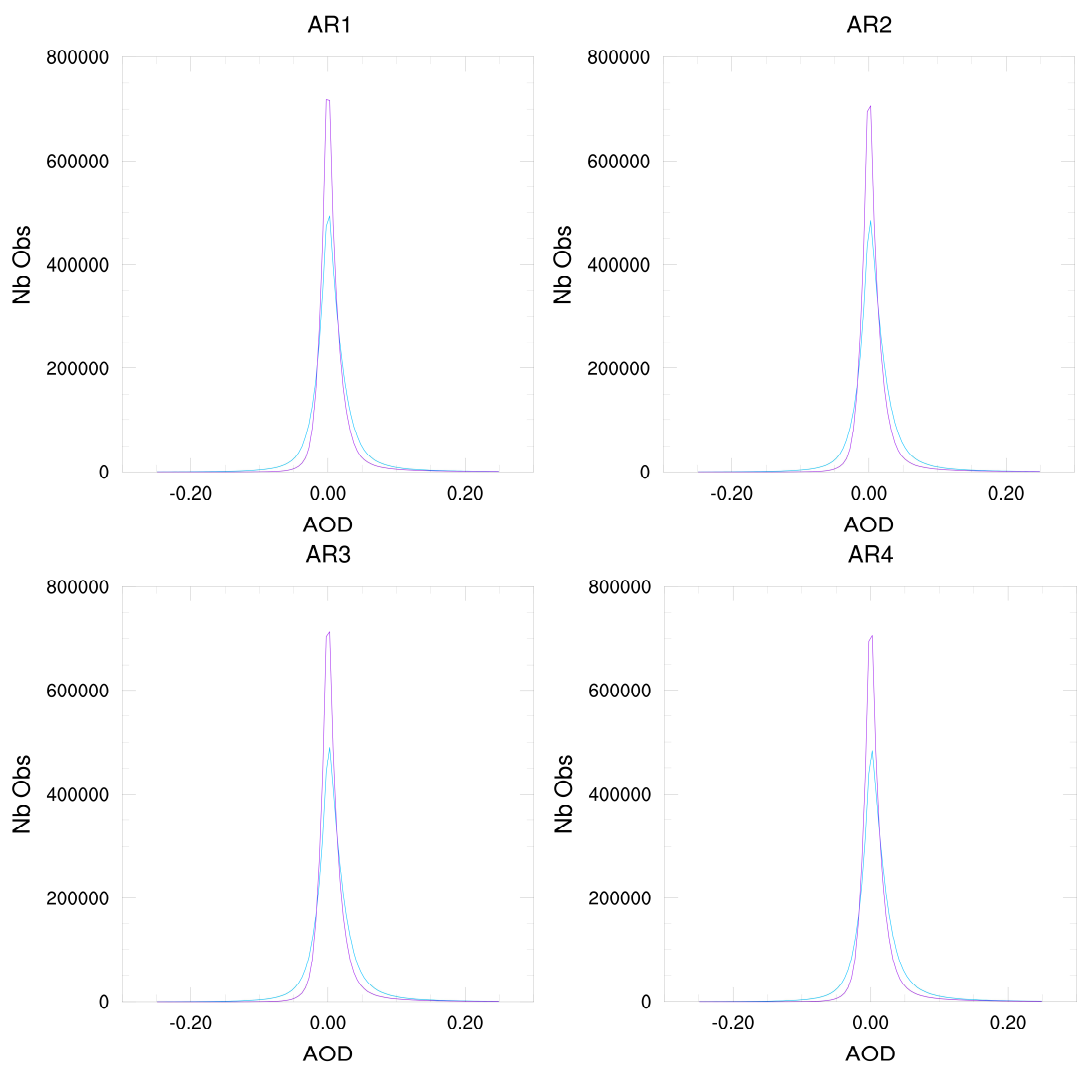
Figure 10: Histograms of differences between synthetic observations and forecast fields (blue) and between synthetic observations and analyzed field (purple) for the four assimilation runs.
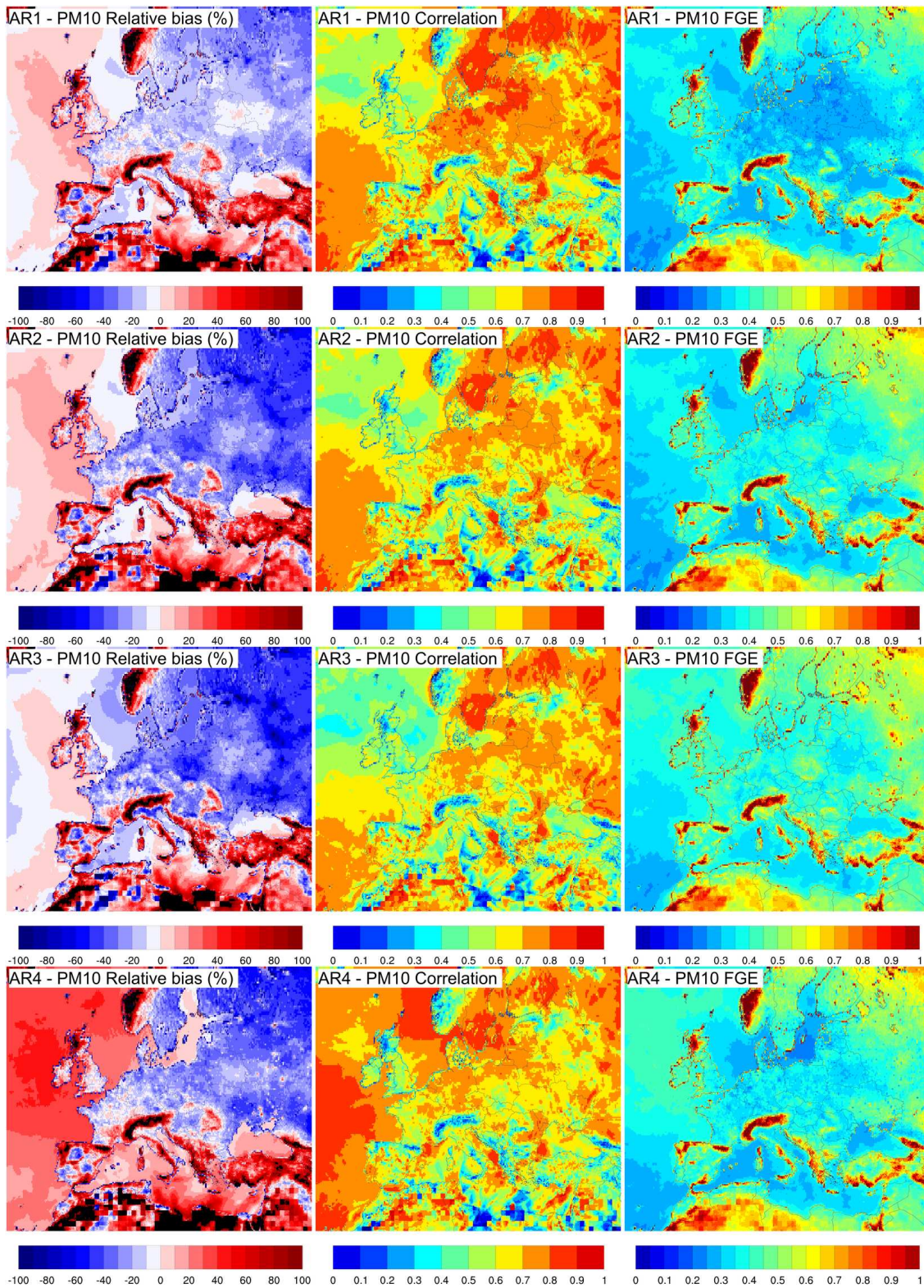
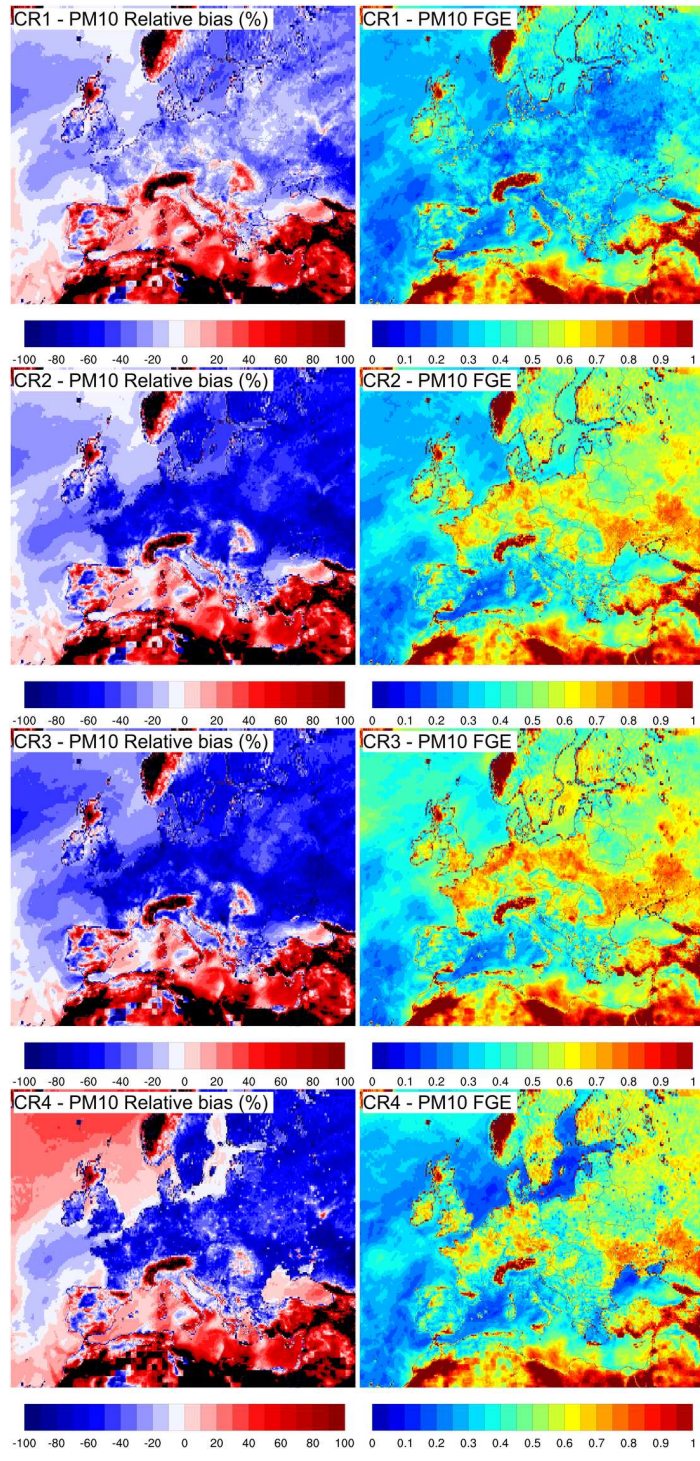**Figure 11: Same legend as Figure 9, for assimilation runs (AR) instead of control runs (CR).**
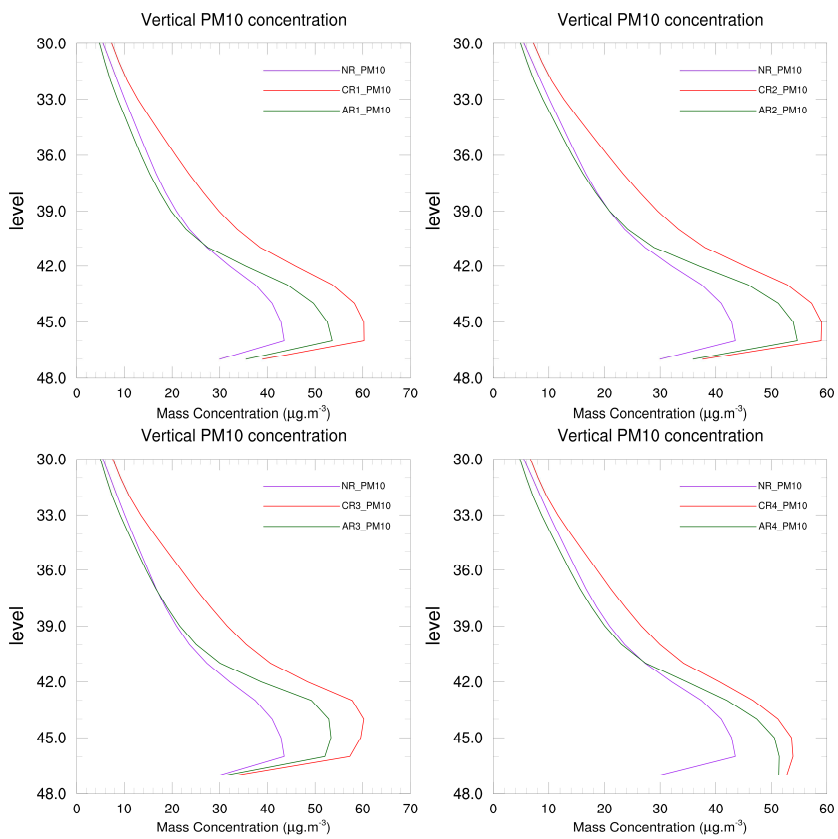
Figure 12: Mean vertical profile, from January to April, over the domain of the concentrations (µg.m^{-3}) of PM$_{10}$ for the 4 set of simulations (1 in top left, 2 in top right, 3 in down left and 4 in down right). The NR is in purple, the CR is in red and the AR is in green.

37
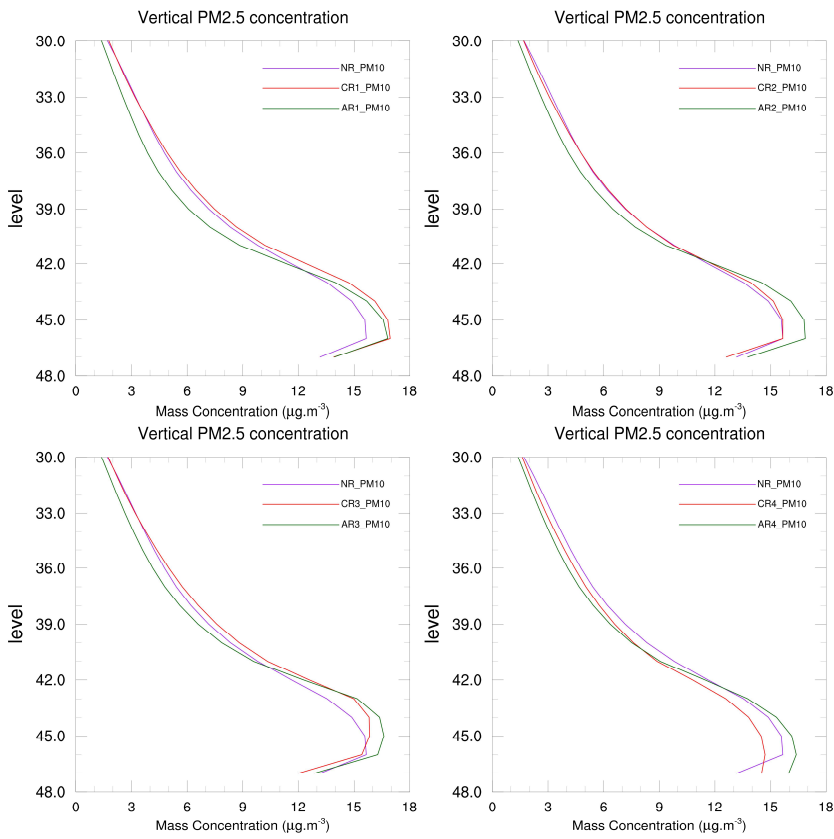
Figure 13: Mean vertical profile, from January to April, over the domain of the concentrations (µg.m^{-3}) of PM$_{2.5}$ for the 4 set of simulations (1 in top left, 2 in top right, 3 in down left and 4 in down right). The NR is in purple, the CR is in red and the AR is in green.
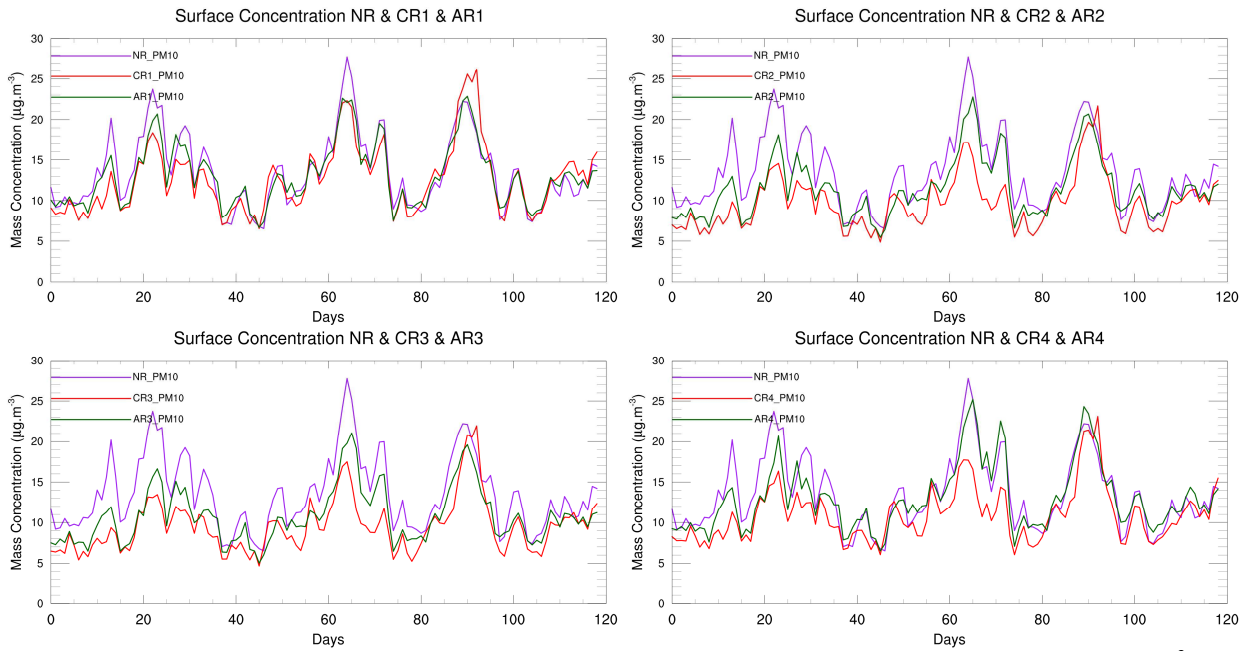
Figure 14: Median values over the AQeR station locations of the daily mean PM$_{10}$ surface concentration (µg.m^{-3}) for the NR (in purple) and the different CR (red) & AR (green) simulations (CR-AR-1 top left, CR-AR-2 top right, CR-AR-3 down left, CR-AR-4 down right).
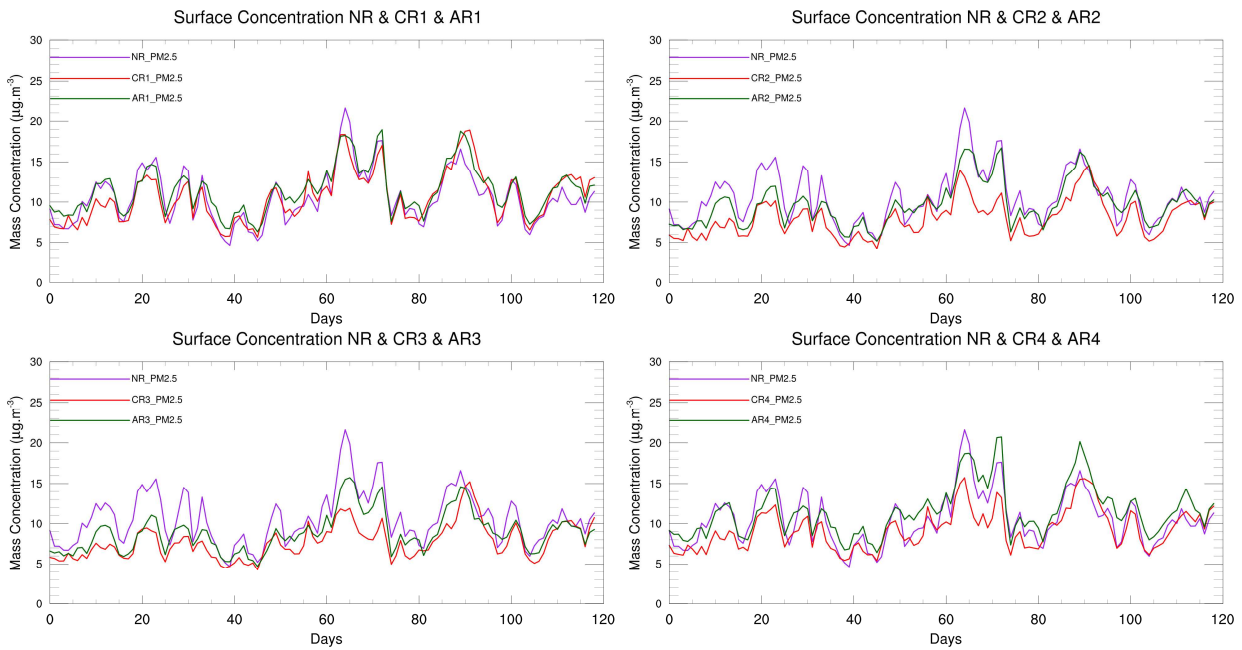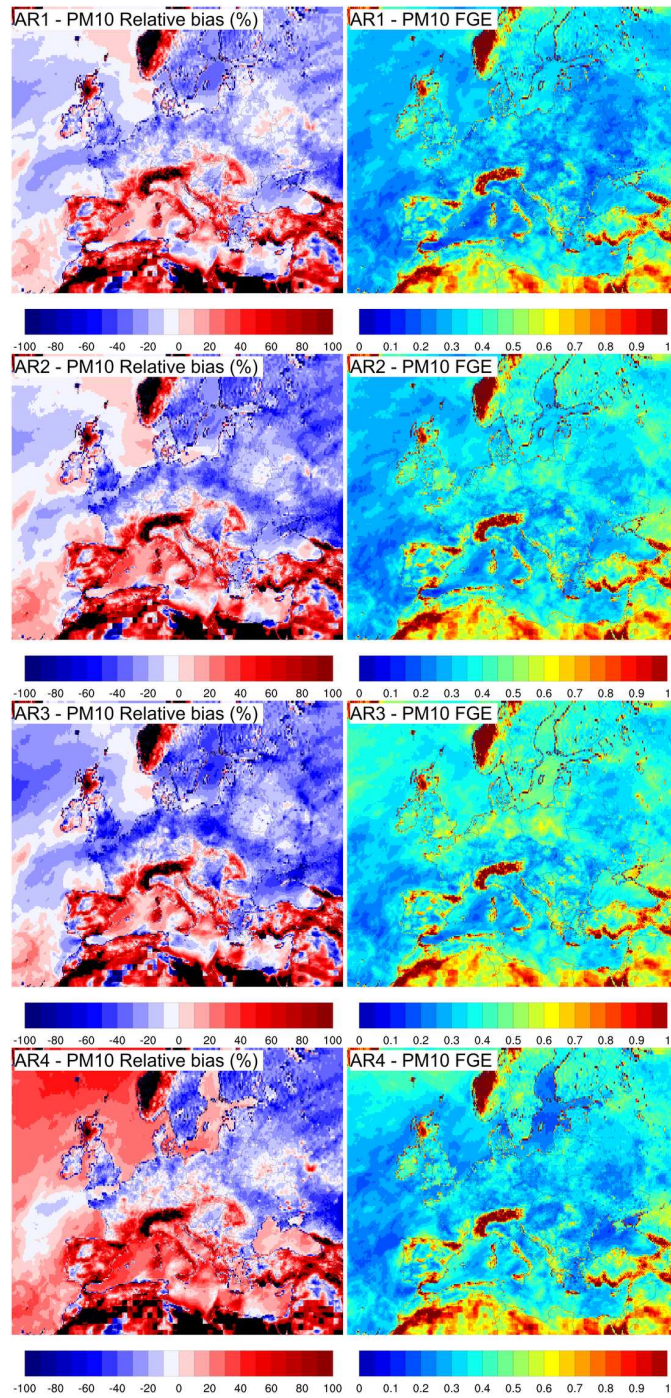

Figure 15: Same legend as Figure 14 for PM$_{2.5}$ concentrations.

Figure16: PM$_{10}$ comparison between the NR and the CRs from the 7th March to the 15th March 2014: relative bias and fractional gross error.

Figure 17: Same legend as Figure 16 for assimilation runs (AR) instead of control runs (CR).
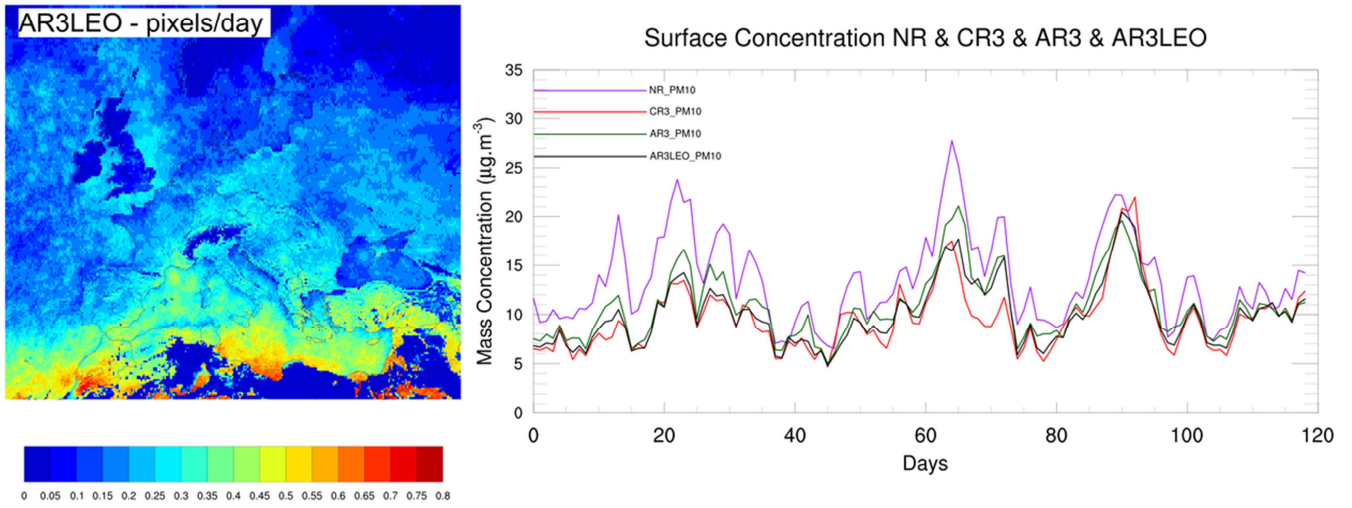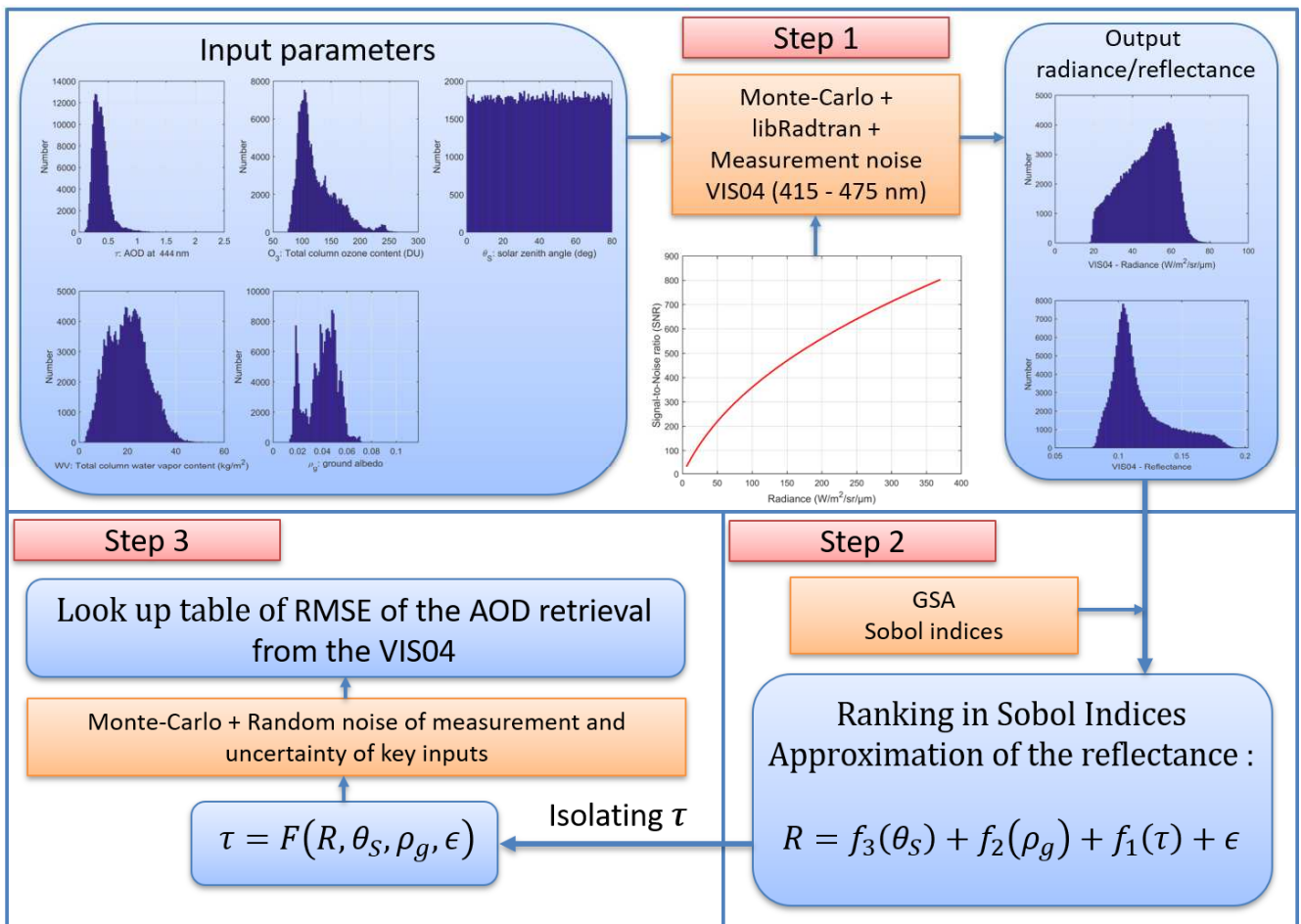
Figure 18 : Results of the assimilation run AR3LEO: density of assimilated synthetic observations (upper-left panel, to be compared with Figure 6), time series of concentration of PM$_{10}$ at surface for NR, CR3, AR3, AR3LEO (upper-right panel) between 1st January and 30th April 2014, PM$_{10}$ relative bias and FGE of AR3LEO from 7 to 14 March 2014 (to be compared with Figure 17).

Figure A1: Summary of the methodology to derive the RMSE of AOD from the FCI reflectance simulator. Step 1 is the computation of FCI radiance. Input parameters are the histograms of AOD, ozone total column, total water vapor content, ground albedo and solar zenithal angle. The libRadtran simulator simulates the distribution of radiance and reflectance in the VIS04 channel and takes into account the signal-to-noise ratio of FCI. Step 2 is the approximation of the reflectance in functions of key parameters using a Global Analysis Sensitivity method and Sobol indices. Step 3 is the retrieval of the AOD RMSE using random noise of measurement and the uncertainty of key parameters.